

Realizing Highly Efficient Sonodynamic Bactericidal Capability through the Phonon–Electron Coupling Effect Using Two-Dimensional Catalytic Planar Defects

Congyang Mao, Wanyu Jin, Yiming Xiang, Yizhou Zhu, Jun Wu, Xiangmei Liu, Shuilin Wu, Yufeng Zheng, Kenneth M. C. Cheung, and Kelvin Wai Kwok Yeung*


Conferring catalytic defects in sonosensitizers is of paramount importance in reinforcing sonodynamic therapy. However, the formation of such 0D defects is governed by the Schottky defect principle. Herein, 2D catalytic planar defects are designed within Ti_3C_2 sheets to address this challenge. These specific planar slip dislocations with abundant Ti^{3+} species ($\text{Ti}_3\text{C}_2\text{-SD}(\text{Ti}^{3+})$) can yield surface-bound O due to the effective activation of O_2 , thus resulting in a substantial amount of $^1\text{O}_2$ generation and the $99.72\% \pm 0.03\%$ bactericidal capability subject to ultrasound (US) stimulation. It is discovered that the 2D catalytic planar defects can intervene in electron transfer through the phonon drag effect—a coupling effect between surface electrons and US-triggered phonons—that simultaneously contributes to a dramatic decrease in O_2 activation energy from 1.65 to 0.06 eV. This design has achieved a qualitative leap in which the US catalytic site has transformed from 0D to 2D. Moreover, it is revealed that the electron origin, electron transfer, and visible O_2 activation pathway triggered by US can be attributed to the phonon–electron coupling effect. After coating with neutrophil membrane (NM) proteins, the $\text{NM-Ti}_3\text{C}_2\text{-SD}(\text{Ti}^{3+})$ sheets further demonstrate a 6- \log_{10} reduction in methicillin-resistant *Staphylococcus aureus* burden in the infected bony tissue.

ROS can induce lipid membrane peroxidation, DNA/protein disruption, and cellular oxidative stress, thereby resulting in consequent bacterial cell death.^[4] Harnessing the powerful tissue penetration depth (≈ 10 cm) of US,^[5] SDT has therefore been promising as an alternative to phototherapy in eradicating deep-seated infections. In fact, SDT has been successfully applied clinically in the treatment of metastasized pathological breast cancer and terminal breast cancer.^[6,7] However, when SDT is used in clinical therapy, most of the currently available sonosensitizers, which are comprised of organic small molecules, are compromised because of the off-target effect, poor excretion rate, and bio-incompatibility.^[8,9] Alternatively, inorganic sonosensitizers feature unique physiochemical properties and chemical stability, rendering them more promising candidates for SDT.^[10,11] However, most inorganic sonosensitizers present low ultrasonic absorption efficiency, fast electron–hole recombination, and dose-dependent toxicity.^[12,13] For example, titanium dioxide (TiO_2), a paradigm of inorganic sonosensitizer, has a relatively low quantum yield of US-triggered ROS due to its fast electron–hole recombination (50 ± 30 ns).^[14,15] Thus, the development of an inorganic sonosensitizer that facilitates highly efficient SDT is challenging.

1. Introduction

Sonodynamic therapy (SDT), as a non-invasive therapeutic approach, takes advantage of exogenous ultrasound (US) to trigger sonosensitizers to react with surrounding O_2 and even water molecules to elicit reactive oxygen species (ROS).^[1–3]

C. Mao, W. Jin, Y. Xiang, Y. Zhu, K. M. C. Cheung, K. W. K. Yeung
Department of Orthopaedics & Traumatology
Li Ka Shing Faculty of Medicine
The University of Hong Kong
Pokfulam, Hong Kong 999077, China
E-mail: wkkyeung@hku.hk

 The ORCID identification number(s) for the author(s) of this article can be found under <https://doi.org/10.1002/adma.202208681>.

© 2023 The Authors. Advanced Materials published by Wiley-VCH GmbH. This is an open access article under the terms of the Creative Commons Attribution-NonCommercial-NoDerivs License, which permits use and distribution in any medium, provided the original work is properly cited, the use is non-commercial and no modifications or adaptations are made.

DOI: 10.1002/adma.202208681

C. Mao, W. Jin, Y. Xiang, Y. Zhu, J. Wu, K. M. C. Cheung, K. W. K. Yeung
Shenzhen Key Laboratory for Innovative Technology in Orthopaedic Trauma
Department of Orthopaedics and Traumatology
The University of Hong Kong-Shenzhen Hospital
Shenzhen 518053, China

X. Liu
School of Life Science and Health Engineering
Hebei University of Technology
Xiping Avenue 5340, Beichen District, Tianjin 300401, China
S. Wu, Y. Zheng
School of Materials Science and Engineering
Peking University
Beijing 100871, China

The literature has identified that the establishment of isolated Schottky defects plays a decisive role in the promotion of electron mobility and inhibition of electron–hole recombination in Ti-based photocatalysis and sonocatalysis.^[16–18] Unfortunately, such point defects governed by the Schottky defect principle can only sit on 0D, in which the efficiency of US-mediated ROS generation has been significantly reduced.^[16,17] Hence, we hypothesize that a new design of catalytic defects arranged in a 2D plane could substantially convert O₂ to singlet oxygen (¹O₂), thereby achieving highly efficient SDT. Additionally, ¹O₂ is a common product of the reduction reaction between electrons and O₂ molecules during the SDT process.^[19,20] Therefore, a better understanding of electron origin, electron transfer, and the reaction pathway between electrons and O₂ under US radiation may aid in the development of an effective sonosensitizer. The O₂ activation energy (*E*_{act}) barrier on the surface of the sonosensitizer would also determine the efficiency of O₂ reduction reaction and SDT.^[21]

Ti₃C₂, a transition metal carbide (MXene), is a potential candidate for a Ti-based sonosensitizer, since its photocatalytic properties and metallic electrical conductivity are superior to others.^[22,23] However, pristine Ti₃C₂ exhibits ultrasonic silence due to the absence of crystal defects. Considering the special 2D structure of Ti₃C₂,^[24] we propose to create 2D catalytic planar defects on Ti₃C₂ by shifting its Ti atoms on the entire 2D plane under a strong stress field. In this study, we demonstrated that the 2D catalytic planar defects in Ti₃C₂ [Ti₃C₂-SD(Ti³⁺)] sheets, which contain an abundance of Ti³⁺ species, can dramatically produce ¹O₂ upon US stimulation because of the strong phonon–electron coupling effect. The ab initio molecular dynamics (AIMD) analysis revealed that a substantial number of electrons transferred from those 2D catalytic planar defects were induced by the phonons emitted due to ultrasonic mechanical wave-induced lattice vibration. The 2D planar defects have realized the acceleration of electron transfer and the reduction of the *E*_{act} barrier to O₂–surface reaction, thereby resulting in superior ¹O₂ generation through the reduction reaction between the O₂ and the electrons (Figure 1).

We then decorate the Ti₃C₂-SD(Ti³⁺) nano-sheets with neutrophil membrane (NM) proteins through electrostatic adsorption to clinically exhibit the bactericidal capability of this new 2D sonosensitizer.^[25] The NM-coated Ti₃C₂-SD(Ti³⁺) biomaterials can capture the bacteria precisely and eliminate them through the release of ¹O₂ upon US stimulation (Figure 1). In general, the newly designed 2D sonosensitizer presents robust antibacterial efficacy in the treatment of bony tissue infection induced by methicillin-resistant *Staphylococcus aureus* (MRSA). Our invention unveils the phonon–electron coupling effect that provides unique insights to the design of sonosensitizers. Such a highly efficient, multifunctional, and biocompatible neutrophil-mimicking Ti₃C₂-SD(Ti³⁺) sonosensitizer provides a promising clinical alternative for SDT in the future.

2. Experimental Section

2.1. Materials

Ti₃AlC₂ MAX powder with a purity of 99.5% (200 mesh) was purchased from the Jinghuarui Chemical Glass Instrument company. Hydrofluoric acid (40%), dimethyl sulfoxide (DMSO, 99.5%), ethanol (99.5%), *N,N*-dimethylformamide (DMF), and anhydrous sodium sulfate (95%) were purchased from Sinopharm Chemical Reagent. chitosan (CS) (viscosity: 100–200 mPa s, 179.17 MW), 1,3-diphenylisobenzofuran (DPBF) (#D122454), thiazolyl blue tetrazolium bromide (MTT), 2-nitrophenyl-β-D-galactopyranoside (ONPG), and isopropyl β-D-1-thiogalactopyranoside (IPTG) were obtained from Aladdin Regents. Lipopolysaccharides (LPS), tris-HCl, d-mannitol, sucrose, EGTA, EDTA, 5,5-dimethyl-1-pyrroline-*N*-oxide (DMPO), and 2,2,6,6-tetramethylpiperidine (TEMP) were obtained from Sigma-Aldrich. Red blood cell (RBC) lysis buffer and a protease and phosphatase inhibitor cocktail were purchased from Thermo Fisher Scientific. The live and dead bacterial staining kit (#40274ES60), 4',6-diamidino-2-phenylindole

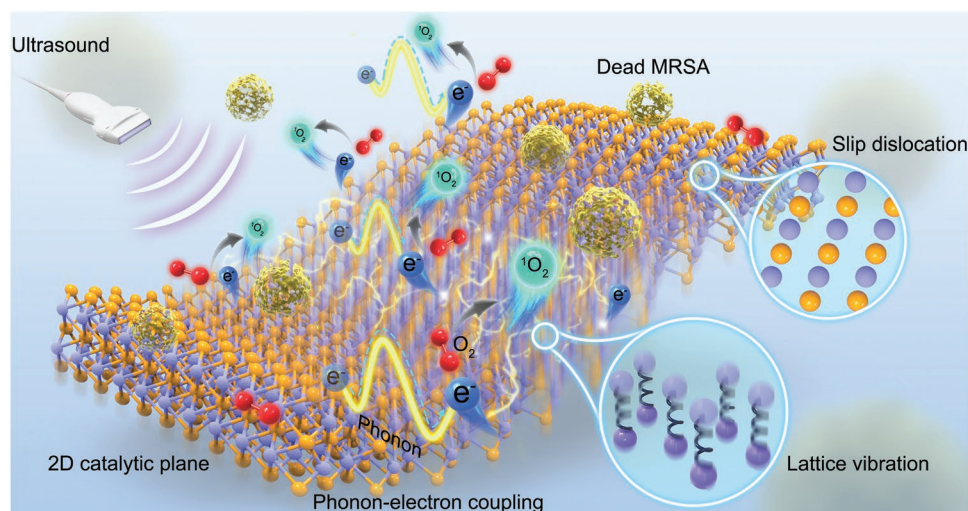


Figure 1. Mechanism and antibacterial performance of 2D catalytic planar defects-mediated SDT. Slip dislocation, as the catalytic site, emits large numbers of phonons through ultrasound-induced violent lattice vibrations. The phonons then drag the electrons and promote electron transfer through the phonon–electron coupling effect, significantly lowering the energy barrier for the REDOX reaction between electrons and oxygen and boosting singlet oxygen (¹O₂) generation for highly efficient MRSA eradication.

(DAPI) stain solution (5 mg mL⁻¹) (#40728ES03), and fluorescein isothiocyanate (FITC)-conjugated phalloidin (#40735ES75) were bought from Yeasen Biotech. The enhanced BCA protein assay kit (#P0010), enhanced ATP assay kit (#S0027), and ROS assay kit (#S0033) were purchased from the Beyotime Institute of Biotechnology. The ALP assay kit (#A059-2-2) was obtained from Nanjing Jiancheng Bioengineering Institute. The total RNA kit I (#R6834-02) was purchased from Omega Bio-tek. The PrimeScript RT master mix (Perfect Real Time) (#RR036B) and TB Green premix ex taq II (Tli RNaseH Plus) (#RR820B) were purchased from TaKaRa Bio. The mouse nitric oxide synthase 2/inducible nitric oxide synthase (iNOS) enzyme-linked immunosorbent assay (ELISA) Kit (#E-EL-M0696c), mouse tumor necrosis factor-alpha (TNF- α) ELISA kit (#E-EL-M0049c), mouse arginase I (Arg-1) ELISA kit (#E-EL-M0154c), and mouse interleukin (IL)-10 ELISA kit (#E-EL-M0046c) were obtained from Elabscience Biotechnology. Anti-iNOS antibody (#bs-0162R) was obtained from Bioss and anti-TNF- α antibody (#BA0131) was obtained from Boster Biological Technology. Anti-Runx-2 antibody (#12556) was purchased from Cell Signaling Technology. Anti-IL-10 antibody (#DF6894) and anti-collagen I antibody (#AF7001) was purchased from Affinity Biosciences. Anti-ARG1 antibody (#16001-1-AP) and anti-OPN antibody (#22952-1-AP) was purchased from Proteintech Group.

2.2. Preparation of Ti₃C₂

Ti₃AlC₂ MAX powder (5 g) was slowly added to 50 mL of 40% hydrofluoric acid solution and etched under magnetic stirring at a low velocity. After 24 h, the mixture was successively washed with deionized water and ethanol three times in a centrifuge at a speed of 8000 rpm. 5 min later, the product was immersed in 50 mL of DMSO solution and magnetically stirred for 36 h. Then, the obtained mixture was successively washed with deionized water and ethanol three times and freeze-dried to obtain the final product of Ti₃C₂ powder.

2.3. Preparation of Ti₃C₂-SD(Ti³⁺)

The Ti₃C₂ powder (0.5 g) was dispersed in 60 mL of ethanol. Then, the mixture was continually inlet with nitrogen and stripped in an ice bath for 4 h using an ultrasonic generator (YQ-1003, Yi Jing Ultrasonic Instrument, Shanghai, China) at 1500 W ultrasonic power. Thereafter, the mixture was removed into a polytetrafluoroethylene container and supplemented with ethanol to reach a volume of 80 mL. After conducting with solvothermal treatment at 120 °C for 16 h in the miniature magnetic high-pressure reaction kettle (#1003, Yushen Instrument, Shanghai, China), the obtained solution was washed three times with ethanol in the centrifuge at 8000 rpm and freeze-dried to harvest the Ti₃C₂-SD(Ti³⁺) powder.

2.4. Activation and Collection of Neutrophils

The neutrophils were collected from the whole blood of male BALB/C mice (6 weeks old) with reference to a modified Percoll

gradient method.^[25] Before the collection of whole blood, mice were injected intraperitoneally with 1.5 mg kg⁻¹ of LPS to activate the neutrophils. Then, whole blood was obtained from LPS-treated mice by heart puncture 6 h later. After being centrifuged at 3220 × g for 5 min (4 °C), the buffy coat was collected and slowly added to the mixture of 52%, 69%, and 78% v/v Percoll solution (in phosphate buffer saline [PBS]). The mixture was then centrifuged at 1500 × g for 30 min (4 °C) and the sample was collected from the interface of 69% and 78% Percoll layers and the upper part of the 78% Percoll layer. The sample was treated with RBC lysis buffer to lyse the erythrocytes and the obtained neutrophils were washed with PBS for purification and stored at -80 °C.

2.5. Derivation of Neutrophil Membrane Proteins

NM proteins were harvested following a previously published protocol.^[25] The neutrophils stored at -80 °C were unfrozen, washed with PBS and resuspended in hypotonic lysis buffer supplemented with Tris-HCl (30 mM, pH = 7.5), sucrose (75 mM), d-mannitol (225 mM), EDTA (0.2 mM), and cocktail. NM was obtained by centrifuging the mixture successively under the following conditions: 3500 × g for 5 min (4 °C) to separate the intact cells and the nuclei, 20 000 × g for 25 min (4 °C) to separate the mitochondria, and 100 000 × g for 35 min (4 °C) to obtain the NM. Finally, the NM was washed with 0.2 mM of EDTA and resuspended in 0.2 mM of EDTA solution added to cocktail. The content of NM was determined using a commercial BCA protein assay kit.

2.6. Preparation of NM-Ti₃C₂-SD(Ti³⁺)

NM-modified Ti₃C₂-SD(Ti³⁺) (NM-Ti₃C₂-SD(Ti³⁺)) was obtained by simple electrostatic adsorption. Briefly, Ti₃C₂-SD(Ti³⁺) powder (50 mg) was dispersed in 50 mL of deionized water. Then, CS (20 mg) was slowly added to the Ti₃C₂-SD(Ti³⁺) suspension and magnetically stirred for 1 h. After washing with deionized water three times, the Ti₃C₂-SD(Ti³⁺) absorbed with CS (CS-Ti₃C₂-SD(Ti³⁺)) was obtained and dispersed in 50 mL of deionized water again. Freeze-dried NM (5 mg) was then dispersed in 5 mL of deionized water and slowly added to the CS-Ti₃C₂-SD(Ti³⁺) suspension under a magnetic stir. After 1 h, the product was washed with deionized water three times and freeze-dried to obtain NM-Ti₃C₂-SD(Ti³⁺) powder.

2.7. Characterization

A field-emission scanning electron microscopy (SEM) (ZEISS Sigma 500, ZEISS, Oberkochen, Germany) was used to observe the surface morphologies of the samples. A field-emission high resolution transmission electron microscope (HRTEM) (JEM-2100F, JEOL, Tokyo, Japan) with an EDAX Elite T spectrometer was applied to obtain HRTEM images and energy dispersive X-ray spectroscopy (EDX) elemental mapping. The phase structure of the samples was analyzed by the X-ray diffraction (XRD) (Bruker D8A A25, Bruker, Karlsruhe, Germany) in continuous

mode scanning from 5° to 80° with a step size of 4° min⁻¹. Cu K α radiation was applied as the radiation source ($\lambda = 1.5406 \text{ \AA}$) at 40 kV and 30 mA. The element composition and chemical valence of the samples were analyzed using X-ray photoelectron spectroscopy (XPS) (Thermo Scientific ESCALAB 250Xi, Thermo Scientific, Wilmington, USA). The chemical structures were analyzed using Fourier transform infrared spectroscopy (FTIR) (Nicolet 570). Electron spin resonance (ESR) (JES-FA200, JEOL) was used to detect oxygen vacancy and ROS generation. The current density and electrochemical impedance spectroscopy (EIS) were measured with the indium tin oxide glass on an electrochemical workstation (CHI660E, Chenhua Instrument, Shanghai, China) in a standard three-electrode system. The ζ -potential and hydraulic diameter of the samples were detected by a Zetasizer Nano series Nano-ZS (Malvern Instruments, Malvern, UK) at room temperature.

2.8. Ab Initio Molecular Dynamics Analysis

In this work, the first-principle calculation steps were completed through structural optimization, static self-consistent field, density of state calculation, and charge calculation. All calculation steps were completed by VASP-6.1.0, combined with the PBE functional under the generalized gradient approximation in the frame of density functional theory (DFT) with D3 dispersion correction, combined with the projector augmented wave. The plane wave cut off energy was 500 eV. Among them, K point adopted the density of $3 \times 3 \times 1$. The free energy surface and oxygen splitting trajectory adopted the slow-growth method, and the sampled data averaged 20 AIMD trajectories of 50 ps in 300 K. In addition, the trajectory picture was drawn using VMD-1.9.3.

2.9. Detection of ROS

DPBF was used to detect singlet oxygen ($^1\text{O}_2$), which could react with $^1\text{O}_2$ and exhibit a declined absorption at 420 nm. Briefly, DPBF was dissolved in a DMF solution to prepare the working solution at a concentration of 100 $\mu\text{g mL}^{-1}$. Then, a 100 μL sample (500 $\mu\text{g mL}^{-1}$) was slowly added to 100 μL of working solution in a 2 mL EP tube. The mixture was balanced in the dark for 10 min and then treated ultrasonically (1.0 MHz, 1.5 W cm^{-2} , 50% duty cycle) for another 10 min. The absorption spectra of the mixture from 350 to 500 nm were detected every 1 min. An ESR spectrometer was also used to detect the production of ROS. Briefly, a 100 μL sample (500 $\mu\text{g mL}^{-1}$) was added to 50 mM of TEMP solution for $^1\text{O}_2$ detection or added into 0.1 M of DMPO for hydroxyl radicals ($\cdot\text{OH}$) trapping. The mixture was balanced in the dark for 10 min and then treated ultrasonically (1.0 MHz, 1.5 W cm^{-2} , 50% duty cycle) for 1 min. ESR spectra were obtained from the ESR spectrometer at a micro-frequency of 8.93 GHz and a micropower of 3 mW.

2.10. In Vitro Antibacterial Test

The antibacterial activity of $\text{Ti}_3\text{C}_2\text{-SD}(\text{Ti}^{3+})$ and $\text{NM-Ti}_3\text{C}_2\text{-SD}(\text{Ti}^{3+})$ against MRSA (ATCC 43300) was evaluated using

a plate counting method. First, 100 μL of MRSA suspension (10^8 CFU mL^{-1}) was added to the 2 mL EP tubes. Then 100 μL of normal saline, $\text{Ti}_3\text{C}_2\text{-SD}(\text{Ti}^{3+})$ suspension (500 $\mu\text{g mL}^{-1}$), or $\text{NM-Ti}_3\text{C}_2\text{-SD}(\text{Ti}^{3+})$ (500 $\mu\text{g mL}^{-1}$) suspension was added to the bacteria, and the mixture was treated with or not treated by US (1.0 MHz, 1.5 W cm^{-2} , 50% duty cycle) for 10 min. Bacteria treated with normal saline were set as the control group. After different treatments, the MRSA suspension was diluted with Luria–Bertani (LB) medium (1:1000) and 20 μL of the diluent was coated on an LB agar plate and cultured at 37 °C for 24 h. The antibacterial ratio was evaluated by the number of colonies formed and calculated using the following formula:

$$\text{Antibacterial ratio (\%)} = (A - B) * 100 / A \quad (1)$$

“A” represented the number of colonies formed on the LB agar plate in the control group, while “B” represented the number of colonies in the experimental group.

Live/dead staining for bacteria was then performed according to the protocols of a commercial assay kit. Briefly, the preliminary procedure was the same as plate counting method. Next, 1 μL of live/dead fluorescent dye was added into US-treated MRSA suspension (100 μL). The mixture was incubated in the dark for 5 min. 10 μL of mixture was collected and then placed on a glass slide. After naturally dried, the treated MRSA cells were examined using a fluorescent microscope (IFM, IX73, Olympus, Tokyo, Japan).

In addition, the SEM was used to observe the integrity of the bacterial membrane. Briefly, the preliminary procedure was the same as plate counting method. The US-treated MRSA cells were then fixed with 2.5% glutaraldehyde for 2 h and dehydrated in gradient ethanol solution (30%, 50%, 70%, 90%, and 100%) for 15 min each. Finally, the samples were air-dried and observed under SEM.

2.11. Synthesis of Cy5.5-Sheets and Flow Cytometry of Sheets Adhered to MRSA

The Cy5.5 was combined with sheets by the simple electrostatic adsorption. Briefly, 2 μL Cy5.5 (1 mM) was mixed with 2 mL $\text{Ti}_3\text{C}_2\text{-SD}(\text{Ti}^{3+})$ (500 $\mu\text{g mL}^{-1}$) or $\text{NM-Ti}_3\text{C}_2\text{-SD}(\text{Ti}^{3+})$ (500 $\mu\text{g mL}^{-1}$). The mixture was stirred for 3 h and then washed with hot ultrapure water for three times. Next, MRSA bacteria were washed three times with PBS. The MRSA bacteria were further mixed with Cy5.5-sheets (500 $\mu\text{g mL}^{-1}$) and incubated at 37 °C for 1 h. Finally, the above mixture was washed again for three times with PBS and resuspended into PBS for flow cytometry (FCM) (FACSAria) analysis.

2.12. Study for Antibacterial Mechanism

2.12.1. Examination of MRSA Membrane Permeability

Membrane permeability was evaluated following a previously published protocol.^[26] MRSA cells were incubated in LB medium supplemented with 10 $\mu\text{g mL}^{-1}$ of IPTG at 37 °C for 24 h. After being centrifuged at 6000 rpm for 5 min, the

precipitation was washed with PBS three times and resuspended in PBS to obtain an MRSA suspension with the desired working concentration ($OD_{600} = 0.05\text{--}0.1$). Then 100 μL of MRSA suspension was added to 2 mL EP tubes followed by the addition of 100 μL of PBS, $\text{Ti}_3\text{C}_2\text{-SD}(\text{Ti}^{3+})$ (500 $\mu\text{g mL}^{-1}$), or $\text{NM-Ti}_3\text{C}_2\text{-SD}(\text{Ti}^{3+})$ (500 $\mu\text{g mL}^{-1}$). The suspension was treated ultrasonically (1.0 MHz, 1.5 W cm^{-2} , 50% duty cycle) for 10 min and 15 μL of the suspension was mixed with 15 μL of ONPG (12.5 mM), 10 μL of DMSO (7%), and 110 μL of PBS in a 96-well plate. The absorbance of the mixture was determined at 420 nm using a microplate reader (SpectraMax i3, Molecular Devices, San Francisco, CA, USA).

2.12.2. Determination of Protein Leakage and ATP Activity

The protein leakage and ATP activity of MRSA cells were determined with an enhanced BCA protein assay kit and an enhanced ATP assay kit, respectively. MRSA cells were incubated in LB medium at 37 $^\circ\text{C}$ for 24 h. After being washed with PBS three times in the centrifuge (6000 rpm, 5 min), the MRSA cells were resuspended in PBS to obtain a suspension with the desired working concentration ($OD_{600} = 0.05\text{--}0.1$). Then 100 μL of MRSA suspension was added to 2 mL EP tubes followed by the addition of 100 μL of PBS, $\text{Ti}_3\text{C}_2\text{-SD}(\text{Ti}^{3+})$ (500 $\mu\text{g mL}^{-1}$), or $\text{NM-Ti}_3\text{C}_2\text{-SD}(\text{Ti}^{3+})$ (500 $\mu\text{g mL}^{-1}$). The suspension was treated ultrasonically (1.0 MHz, 1.5 W cm^{-2} , 50% duty cycle) for 10 min and diluted with 500 μL of PBS. Then, the dilution was centrifuged at 6000 rpm for 5 min to obtain bacterial precipitation. The ATP activity and protein concentration of the precipitation were determined according to the protocols of the commercial assay kits.

2.12.3. Oxidative Stress

The oxidative stress of MRSA cells after treatment with different samples was determined using a ROS Assay Kit. MRSA cells were incubated in LB medium at 37 $^\circ\text{C}$ for 24 h. After being washed with PBS three times in the centrifuge (6000 rpm, 5 min), the MRSA cells were incubated in PBS supplemented with 10 μM 2',7'-dichlorodihydrofluorescein diacetate (DCFH-DA) for 30 min. After being washed with PBS three times in the centrifuge (6000 rpm, 5 min), MRSA cells loaded with DCFH-DA were resuspended in PBS to obtain a suspension with the desired working concentration ($OD_{600} = 0.05\text{--}0.1$). Then 100 μL of MRSA suspension was added to 2 mL EP tubes followed by the addition of 100 μL of PBS, $\text{Ti}_3\text{C}_2\text{-SD}(\text{Ti}^{3+})$ (500 $\mu\text{g mL}^{-1}$), or $\text{NM-Ti}_3\text{C}_2\text{-SD}(\text{Ti}^{3+})$ (500 $\mu\text{g mL}^{-1}$). The suspension was treated ultrasonically (1.0 MHz, 1.5 W cm^{-2} , 50% duty cycle) for 10 min and the relative fluorescence intensity at 525 nm was detected by the microplate reader with an excitation wavelength of 488 nm.

2.13. The Establishment of MRSA Biofilm and Biofilm Disruption Assay

First, 100 μL of MRSA bacterial suspension (10^7 CFU mL^{-1}) was added into the 96-well plates and subsequently cultured for 48 h at 37 $^\circ\text{C}$ to form the MRSA biofilm. The culture media

were changed every 12 h. Afterward, 100 μL of normal saline or $\text{NM-Ti}_3\text{C}_2\text{-SD}(\text{Ti}^{3+})$ (500 $\mu\text{g mL}^{-1}$) suspension was added to the bacteria, and the mixture was treated with US (1.0 MHz, 1.5 W cm^{-2} , 50% duty cycle) for 10 min. Live/dead bacteria staining was then performed according to the protocols of a commercial assay kit.

2.14. Hemolytic Activity Test

The RBCs of mice were collected by refrigerated centrifugation at 3000 rpm for 10 min. Then 500 μL of $\text{Ti}_3\text{C}_2\text{-SD}(\text{Ti}^{3+})$ (500 $\mu\text{g mL}^{-1}$ in saline) and $\text{NM-Ti}_3\text{C}_2\text{-SD}(\text{Ti}^{3+})$ (500 $\mu\text{g mL}^{-1}$ in saline) were incubated with 500 μL of 5% v/v purified mouse RBCs at 37 $^\circ\text{C}$ for 4 h, respectively. Thereafter, the mixture was centrifuged at 3000 rpm for 10 min and the supernatant was collected for the detection of absorbance at 540 nm to evaluate the hemolytic rate. For the positive and negative control groups, 5% v/v purified mouse RBCs were incubated with the same volume of deionized water and normal saline, respectively.

2.15. In Vitro Cytotoxicity Assay

MTT assay was performed to evaluate the toxicity of $\text{Ti}_3\text{C}_2\text{-SD}(\text{Ti}^{3+})$ and $\text{NM-Ti}_3\text{C}_2\text{-SD}(\text{Ti}^{3+})$ to bone marrow mesenchymal stem cells (BMSCs) and monocyte macrophages (RAW 264.7). RAW 264.7 (200 μL , 10^4 cells mL^{-1}) and BMSCs (200 μL , 10^5 cells mL^{-1}) were seeded into 96-well plates. After 1 day, the medium was replaced with 200 μL of fresh medium, $\text{Ti}_3\text{C}_2\text{-SD}(\text{Ti}^{3+})$ (500 $\mu\text{g mL}^{-1}$ in medium) or $\text{NM-Ti}_3\text{C}_2\text{-SD}(\text{Ti}^{3+})$ (500 $\mu\text{g mL}^{-1}$ in medium). Cells cultured in normal medium were set as the control group. The upper medium was changed every 3 days. After culturing for 1, 3, and 7 days, the BMSCs were incubated with 200 μL of MTT solution (0.5 mg mL^{-1} in PBS) for 4 h to form formazan. For RAW 264.7, MTT was evaluated after culturing for 1 and 3 days. Then, the MTT solution was abandoned, and the cells were further incubated with 200 μL of DMF solution under continuous shaking to dissolve the formazan. Finally, the absorbance at 490 nm was determined using a microplate reader. Cell viability was calculated according to the following formula:

$$\text{Cell viability (\%)} = C * 100 / D \quad (2)$$

"C" represented the absorbance at 490 nm in the control group, while "D" represented the absorbance at 490 nm in the experimental group.

After culturing with different samples for 1 day, BMSCs were stained with FITC-conjugated phalloidin and DAPI for filamentous actin and nucleus according to the manufacturer's instructions. The cell morphology was examined using a fluorescent microscope (IFM, IX73, Olympus, Tokyo, Japan).

2.16. Quantitative Real-Time Polymerase Chain Reaction

RAW 264.7 (1 mL, 10^4 cells mL^{-1}) and BMSCs (1 mL, 10^5 cells mL^{-1}) were seeded into 12-well plates. After 1 day,

the medium was replaced with 1 mL of fresh medium, $\text{Ti}_3\text{C}_2\text{-SD}(\text{Ti}^{3+})$ (500 $\mu\text{g mL}^{-1}$ in medium), or $\text{NM-Ti}_3\text{C}_2\text{-SD}(\text{Ti}^{3+})$ (500 $\mu\text{g mL}^{-1}$ in medium). Cells cultured in normal medium were set as the control group. The upper medium was changed every 3 days. After culturing for 1 and 3 days, total RNA was extracted from RAW 264.7 using a Total RNA Kit. For BMSCs, total RNA was extracted after culturing for 7 and 14 days. The RNA concentration of each sample was quantified using a NanoDrop 2000 spectrophotometer (Thermo Scientific, Wilmington, USA). The extracted RNA (500 ng) was reversibly transcribed into cDNA using PrimeScrip RT Master Mix. The quantitative real-time polymerase chain reaction (qRT-PCR) was conducted according to the instructions of TB Green premix ex taq II in CFX Connect real-time system (Bio-Rad, Hercules, CA, USA). The relative protein expression was normalized to glyceraldehyde-3-phosphate dehydrogenase (GAPDH) and analyzed using the $2^{-\Delta\Delta C_t}$ method. The primers used in qRT-PCR are listed in the following Table 1:

2.17. Enzyme-Linked Immunosorbent Assay

RAW 264.7 (1 mL, 10^4 cells mL^{-1}) was seeded into 12-well plates. After 1 day, the medium was replaced with 1 mL of fresh medium, $\text{Ti}_3\text{C}_2\text{-SD}(\text{Ti}^{3+})$ (500 $\mu\text{g mL}^{-1}$ in medium), or

Table 1. The primers used in qRT-PCR experiments.

Cells	Genes	Primer sequences [F, forward; R, reverse; 5'–3']	
RAW 264.7	<i>GAPDH</i>	F: TGAGGTCAATGAAGGGTCTGT R: CCTCGTCCCGTAGACAAAATG	
	<i>iNOS</i>	F: AGCCTGAAGTCATGTTGCGG R: CAACAGGAACCTACCAGCTCACT	
	<i>TNF-α</i>	F: GGTGGTTTGTGAGTGTGAGGGT R: CTCTTCTGTCTACTGAACCTCGGG	
	<i>Arg-1</i>	F: CAGCCCGTCGACATCAAG R: CTGGGGATTGGCAAGGTGAT	
	<i>IL-10</i>	F: AATGCTCCTTGATTTCTGGGC R: TTTAAGGGTTACTTGGGTTGCC	
	<i>CCR7</i>	F: CTATTGGTGATGTTGAAGTTGGC R: ATCATTGCCGTGGTGGTAGTC	
	<i>CD206</i>	F: GGTTCGCATCAGTGAAGGTGG R: CAGGAGGACTGCGTGTTATG	
	BMSCs	<i>GAPDH</i>	F: GCCTCGTCTCATAGACAAGATGTT R: GAAGGCAGCCCTGGTAACC
		<i>OPN</i>	F: TCCTGTCTCCCGTGAAAGT R: GGCTACAGCATCTGAGTGTGTTGC
		<i>OCN</i>	F: AAGCCAGCGACTCTGAGTCT R: CCGGAGTCTATTACCACCTTACT
<i>Runx-2</i>		F: AATGCCTCCGCTGTTATG R: TTCTGTCTGTGCTTCTTG	
<i>COL I</i>		F: CCTGAGCCAGCAGATTGA R: TCCGCTCTCCAGTCAG	
<i>ALP</i>		F: AGCGACACGGACAAGAAGC R: GGCAAAGACCCACATC	
<i>OSX</i>		F: CGGCAAGGCTTCGCATCTG R: GGAGCAGAGCAGACAGGTGAAC	

$\text{NM-Ti}_3\text{C}_2\text{-SD}(\text{Ti}^{3+})$ (500 $\mu\text{g mL}^{-1}$ in medium). Cells cultured in normal medium were set as the control group. After culturing for 1 and 3 days, the concentrations of iNOS, TNF- α , Arg-1, and IL-10 in the medium were determined according to the protocols of the corresponding ELISA Kit.

2.18. Establishment of Bony Tissue Infection Model and Treatment

Animal experiments were approved by the Department of Orthopedics, Union Hospital, Tongji Medical College, Huazhong University of Science and Technology, Wuhan, China (Approval No. S2426). Male BALB/C mice (6 weeks old) were adaptively raised for 7 days (25 ± 2 °C, 60–70% humidity) and then randomly divided into a saline group, control group, $\text{Ti}_3\text{C}_2\text{-SD}(\text{Ti}^{3+})$ group, $\text{NM-Ti}_3\text{C}_2\text{-SD}(\text{Ti}^{3+})$ group, and Vancomycin (Vanco) group ($n = 6$ in each group).

All mice were kept and treated according to the Animal Management Rules of the Ministry of Health of the P. R. of China and the Guidelines for the Care and Use of Laboratory Animals of China. Before surgical procedures, the mice were anesthetized with 2% isoflurane by inhalation, and the right hind legs of the mice were shaved and disinfected. Then, a sterilized scalpel was used to incise the skin and muscle tissue to expose the tibias of the mice. A tunnel bone defect on cortical bone with a diameter of 1 mm was created on the tibia using a medical electric drill. MRSA suspension (2 μL , 1×10^9 CFU mL^{-1}) was injected into the marrow cavities through the defect in order to induce bony tissue infection. After 1 day, the mice in the Vanco group were injected with 5 μL of normal saline, while the mice in the $\text{Ti}_3\text{C}_2\text{-SD}(\text{Ti}^{3+})$ group and the $\text{NM-Ti}_3\text{C}_2\text{-SD}(\text{Ti}^{3+})$ group were injected with 5 μL of $\text{Ti}_3\text{C}_2\text{-SD}(\text{Ti}^{3+})$ (500 $\mu\text{g mL}^{-1}$) and 5 μL of $\text{NM-Ti}_3\text{C}_2\text{-SD}(\text{Ti}^{3+})$ (500 $\mu\text{g mL}^{-1}$), respectively. The mice in the Vanco group were injected with 40 mg kg^{-1} of vancomycin. After different treatments, the defects were sealed with bone wax, while the skin and muscle tissues were carefully sutured. After that, the mice in the saline group, $\text{Ti}_3\text{C}_2\text{-SD}(\text{Ti}^{3+})$ group, and $\text{NM-Ti}_3\text{C}_2\text{-SD}(\text{Ti}^{3+})$ group were treated ultrasonically (1.0 MHz, 1.5 W cm^{-2} , 50% duty cycle) for 10 min.

The mortality of the mice in each group was further recorded throughout the experiments to evaluate the effect of different samples in treating MRSA-induced bony tissue infections. Mice were sacrificed after 14 days of treatment and their blood was collected for routine blood examination. The concentrations of iNOS, TNF- α , Arg-1, and IL-10 in the blood were quantified by ELISA. Moreover, the tibias were photographed to record bacterial infection and bone morphology. A micro-computed tomography ($\mu\text{-CT}$) system (Skyscan 1176, Bruker) was further used to examine bone morphology and new bone formation. H&E and Gram staining were conducted on the bony tissue, and the concentrations of iNOS, TNF- α , Arg-1, and IL-10 were detected by immunofluorescence staining. Immunofluorescence staining for OPN, Runx-2, and COL I was also performed on bony tissue to evaluate the osteogenic activity of different treatments. The bony tissue was also harvested for plate counting experiments.

2.19. Statistical Analysis

All the experimental data were analyzed using mean \pm standard deviation (SD) with $n \geq 3$. The statistical analyses were performed using the GraphPad Prism software, with one-way analysis of variance followed by the Tukey multiple-comparisons test for multiple comparisons and a two-sample Student *t*-test for comparison of two groups. In addition, *p* values of * <0.05, ** <0.01, *** <0.001, and **** <0.0001 were considered statistically significant.

3. Results and Discussion

3.1. The Construction and Acoustoelectric Property of 2D Catalytic Planar Defects

We first fabricated Ti_3C_2 with accordion-like morphology from Ti_3AlC_2 by etching off the Al layers (Figure S1a, Supporting Information).^[27] The original Ti_3C_2 showed multilayer sheets under the SEM and transmission electron microscopy (TEM) observations (Figure S1a,b, Supporting Information). A few-layer Ti_3C_2 with flake-like morphology was then obtained from the ultrasonic exfoliation for 4 h (Figure S1c, Supporting Information). The Ti atomic crystal structure of Ti_3C_2 contains only three layers.^[23] As shown in Figure 2a, the Ti atoms were arranged in a regular parallelogram form (indicated by the black lines in Figure 2b) and observed from the analysis of aberration-corrected high-angle annular dark-field scanning transmission electron microscopy (HAADF-STEM), which is equivalent to the structure reported in the top-view plane of Ti_3C_2 (Figure 2b).^[28] After a one-step strong stress field treatment, the surface morphology of these sheets became rougher than that of pristine Ti_3C_2 (Figure S1d, Supporting Information). The EDX mapping analysis further verified the homogenous distribution of Ti, C, and O elements accordingly (Figure S1e, Supporting Information). In addition, the interlayer distance of the treated Ti_3C_2 sheets gradually increased from 2.9 to 5.2 Å (Figure S1f, Supporting Information). The atomic force microscope analysis further revealed the lamellar structure of treated Ti_3C_2 sheets with the thickness of ≈ 50 nm (Figure S2, Supporting Information). The HAADF-STEM analysis and computer modeling indicated that a planar shift had occurred in the Ti atoms located in the second layer (indicated by reddish-brown balls) with reference to the position of the Ti atoms in the first layer (indicated by blue balls), and this observation was also found in the third layer (indicated by green balls) (Figure 2c,d), thereby resulting in the formation of regular rectangles (indicated by the black lines in Figure 2d) from the parallelogram (Figure 2b), and these 2D catalytic planar defects were comprised of slip dislocation ($\text{Ti}_3\text{C}_2\text{-SD}$, Figure 2c). Interestingly, the shifted Ti atoms in the second layer completely overlapped (indicated by reddish-brown and green overlapping balls) with the Ti atoms in the third layer (Figure 2b,d). The computer-simulated model (i.e., the inset of the top-view plane of $\text{Ti}_3\text{C}_2\text{-SD}$) was verified by the atomic crystal structure in the HAADF-STEM of the modified Ti_3C_2 (Figure 2c,d). Figure 2e presents the XRD patterns of the pristine Ti_3C_2 and the Ti_3C_2 after slip dislocation. Obviously, the $\text{Ti}_3\text{C}_2\text{-SD}$ inherits the XRD characteristics of the pristine

Ti_3C_2 with the shift of (002) diffraction peak (Figure 2f), which might correlate to the structural distortion induced by slip dislocation.^[29,30] The FTIR further revealed that $\text{Ti}_3\text{C}_2\text{-SD}$ inherits the fundamental functional groups of the pristine Ti_3C_2 (Figure S3, Supporting Information).

In fact, the use of vacancy defects to enhance ultrasonic catalytic performance is always preferred.^[16] In accordance with the Schottky defect principle, each vacancy, which is defined as a point defect, results from the escape of an atom from its original equilibrium position when it overcomes the binding energy.^[17] However, such point defects can only produce ROS in low efficiency, subject to US stimulation.^[16] Hence, we proposed shifting the Ti atoms found in the entire 2D plane away from their original positions of equilibrium under the influence of a strong stress field (≈ 50 bar ethanol steam), thus forming 2D catalytic planar defects.

The XPS survey spectra of Ti_3C_2 and $\text{Ti}_3\text{C}_2\text{-SD}$ indicates the presence of Ti, C, O, and F, respectively (Figure S4a, Supporting Information). In the high-resolution Ti 2p (Figure 2g), C 1s, and O 1s (Figure S4b,c, Supporting Information) spectra, the Ti peaks (i.e., Ti-C, C-Ti, O-Ti, and C-Ti-(OH)_x) of $\text{Ti}_3\text{C}_2\text{-SD}$ show slight shift, possibly because of the slip dislocation of Ti atoms.^[30] Interestingly, the obvious peak of *g* value (1.975) in $\text{Ti}_3\text{C}_2\text{-SD}$ was detected by the electron paramagnetic resonance (EPR) test (Figure 2h), which is the typical characteristic peak of Ti^{3+} species,^[31] suggesting that abundant Ti^{3+} species were located in $\text{Ti}_3\text{C}_2\text{-SD}$ ($\text{Ti}_3\text{C}_2\text{-SD}(\text{Ti}^{3+})$). The as-prepared 2D catalytic planar defects-enriched $\text{Ti}_3\text{C}_2\text{-SD}(\text{Ti}^{3+})$ sheets were then uniformly coated on conductive glass for electrochemical testing. EIS showed that a smaller arc radius, followed by a line with a lower slope, was found on $\text{Ti}_3\text{C}_2\text{-SD}(\text{Ti}^{3+})$ (Figure S5, Supporting Information), indicating that a declined charge transfer barrier was successfully established. In addition, the pristine Ti_3C_2 was almost silent under US stimulation, whereas the $\text{Ti}_3\text{C}_2\text{-SD}(\text{Ti}^{3+})$ generated remarkable US-triggered current density (Figure 2i). This observation can be explained by a phenomenon found in US-driven electromotive force generation in semiconductors, namely, the acoustoelectric effect, where it governs the interaction between phonons and free electrons.^[32] According to the phonon drag effect, the ultrasonic wave induces enough crystal lattice vibration in $\text{Ti}_3\text{C}_2\text{-SD}(\text{Ti}^{3+})$ to emit sufficient phonons that strongly coupled with electrons, which facilitated the movement of electrons. Next, an ESR spectrometer was applied to detect ROS generation. The Ti_3C_2 was intrinsically ESR-silent compared to the pure tetramethylpiperidine (TEMP) spin trap. In contrast, the $\text{Ti}_3\text{C}_2\text{-SD}(\text{Ti}^{3+})$ showed three significantly enhanced peak intensities (1:1:1) (Figure 2j), which is a typical characteristic of $^1\text{O}_2$. Moreover, $\text{Ti}_3\text{C}_2\text{-SD}(\text{Ti}^{3+})$ exhibited obvious ultrasonic degradation of DPBF as compared with control (pure DPBF) and pristine Ti_3C_2 (Figure S6a–c, Supporting Information), which further confirmed the US-triggered $^1\text{O}_2$ generation.^[33] Interestingly, the degradation rate of DPBF induced by our 2D catalytic planar defects [$\text{Ti}_3\text{C}_2\text{-SD}(\text{Ti}^{3+})$] was much faster than that induced by the Schottky point defects (sulfur [S]-doped TiO_2 with oxygen deficiency [S- TiO_{2-x}]) under the same ultrasonic intensity and treatment time (Figure S6c–e, Supporting Information),^[34] indicating that the 2D catalytic planar defects are more effective in producing $^1\text{O}_2$ mediated by US.

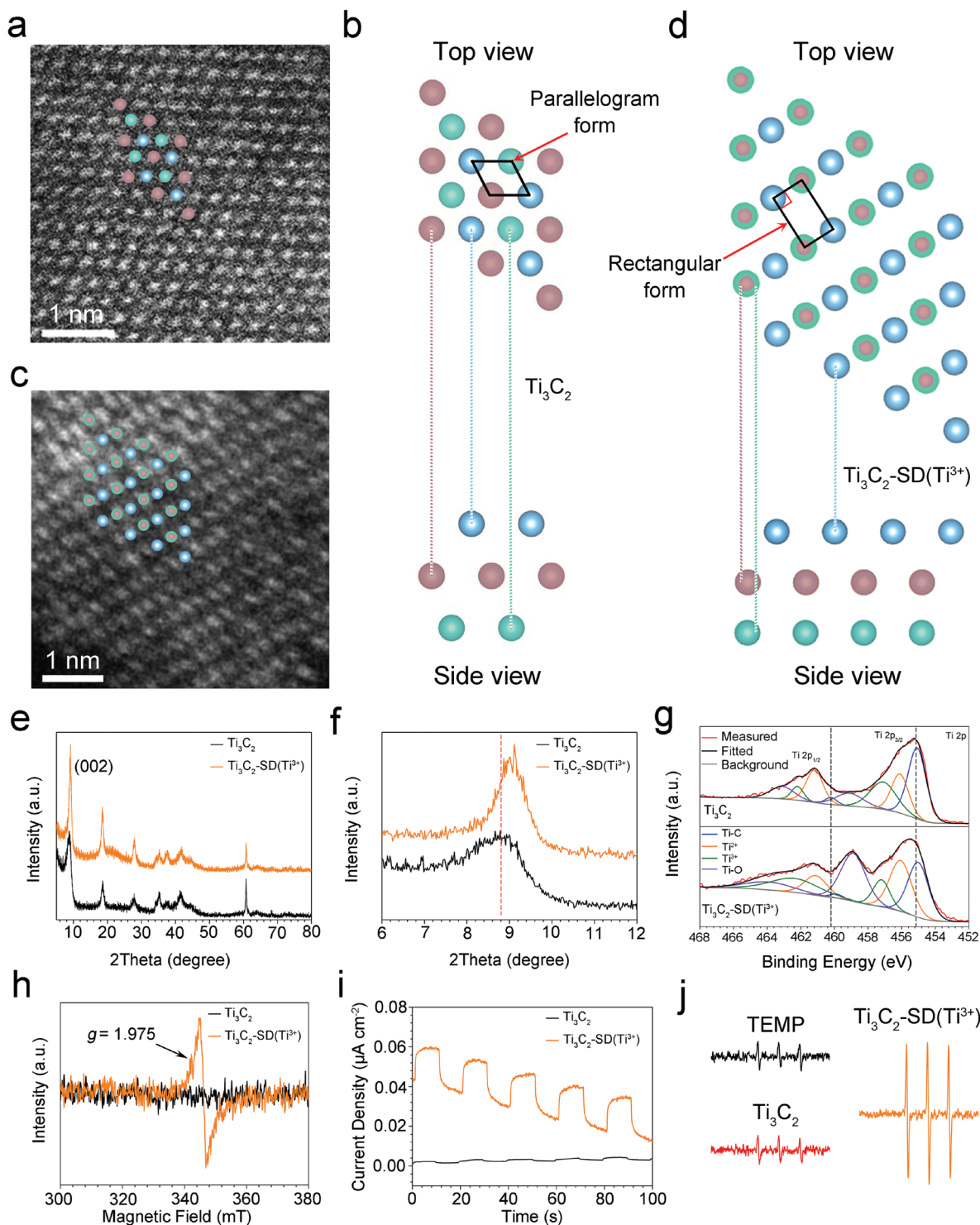


Figure 2. Atomic structure and US-mediated catalytic performance of $\text{Ti}_3\text{C}_2\text{-SD}(\text{Ti}^{3+})$. a) Atomic-resolution HAADF-STEM image of pristine Ti_3C_2 viewed from the top plane. Scale bar: 1 nm. b) Corresponding Ti atomic structure of pristine Ti_3C_2 from the top and side views, respectively. Blue balls: Ti atoms located in the first layer; reddish-brown balls: Ti atoms located in the second layer; green balls: Ti atoms located in the third layer. c) HAADF-STEM image of $\text{Ti}_3\text{C}_2\text{-SD}(\text{Ti}^{3+})$ viewed from the top plane. Scale bar: 1 nm. d) Corresponding Ti atomic structure of $\text{Ti}_3\text{C}_2\text{-SD}(\text{Ti}^{3+})$, showing the formation process of slip dislocation defects. Reddish-brown and green overlapping balls: Ti atoms located in the second and third layers overlap with reference to the position of the Ti atoms in the first layer. From the side view, it was found that the Ti atoms located in the second and third layers slipped with reference to the position of the Ti atoms in the first layer. From the top view, they slipped directly below the center of the parallelogram formed by four Ti atoms in the first layer. e) XRD patterns of the pristine Ti_3C_2 and $\text{Ti}_3\text{C}_2\text{-SD}(\text{Ti}^{3+})$ and f) the corresponding enlarged view of (002) diffraction peak. g) High-resolution XPS spectra of Ti. h) EPR test indicating abundant Ti^{3+} species in $\text{Ti}_3\text{C}_2\text{-SD}(\text{Ti}^{3+})$ sheets. i) Ultrasonic current density performance obtained by adopting five cycles of US on/off. j) ESR test showing the obvious US-mediated $^1\text{O}_2$ generation by $\text{Ti}_3\text{C}_2\text{-SD}(\text{Ti}^{3+})$.

3.2. Phonon–Electron Coupling of the 2D Catalytic Planar Defects

We then used AIMD analysis to figure out the electron origin, electron transfer, and electrons involvement in the activation of oxygen.^[35] The charge density difference was first investigated to reveal the electron's origin (Figure 3a). The cyan and yellow regions represent electron depletion and accumulation, respectively. The carbon (C) atoms were enriched in yellow, while the titanium (Ti) atoms in the first and third layers were surrounded by cyan, illustrating that the 2D catalytic planar defects induced the transfer of electrons from the Ti atoms to the C atoms. Thus, many electrons were enriched on the surface of the C atoms, resulting in the formation of electron origin. Subsequently, electrons were transferred and participated in the activation of oxygen, which was a key step in the

production of $^1\text{O}_2$.^[36] The essence of O_2 activation was from the initial state (IS, gaseous O_2) to the transition state (TS).^[37] The O_2 reaction pathway on the surface of the sheets and the corresponding Gibbs free energy were optimized by DFT calculation (Figure 3b). The O_2 activation energy (E_{act}) of Ti_3C_2 was 0.41 eV, while O_2 E_{act} of $\text{Ti}_3\text{C}_2\text{-SD}(\text{Ti}^{3+})$ was 0.24 eV, indicating that 2D catalytic planar defects-engineered $\text{Ti}_3\text{C}_2\text{-SD}(\text{Ti}^{3+})$ activates O_2 much easier.^[38,39] In the final state (FS), the Gibbs free energy of $\text{Ti}_3\text{C}_2\text{-SD}(\text{Ti}^{3+})$ (0.60 eV) was much lower than that of Ti_3C_2 (1.02 eV), suggesting that the O_2 activation reaction on the surface of $\text{Ti}_3\text{C}_2\text{-SD}(\text{Ti}^{3+})$ was more reliable.

However, the assumption of DFT calculation is under ideal conditions that may result in non-negligible errors.^[40] In a real scenario, the lattice vibration effect during O_2 activation reaction must be considered, especially for US-triggered catalysis. We used AIMD to simulate the real O_2 activation pathway

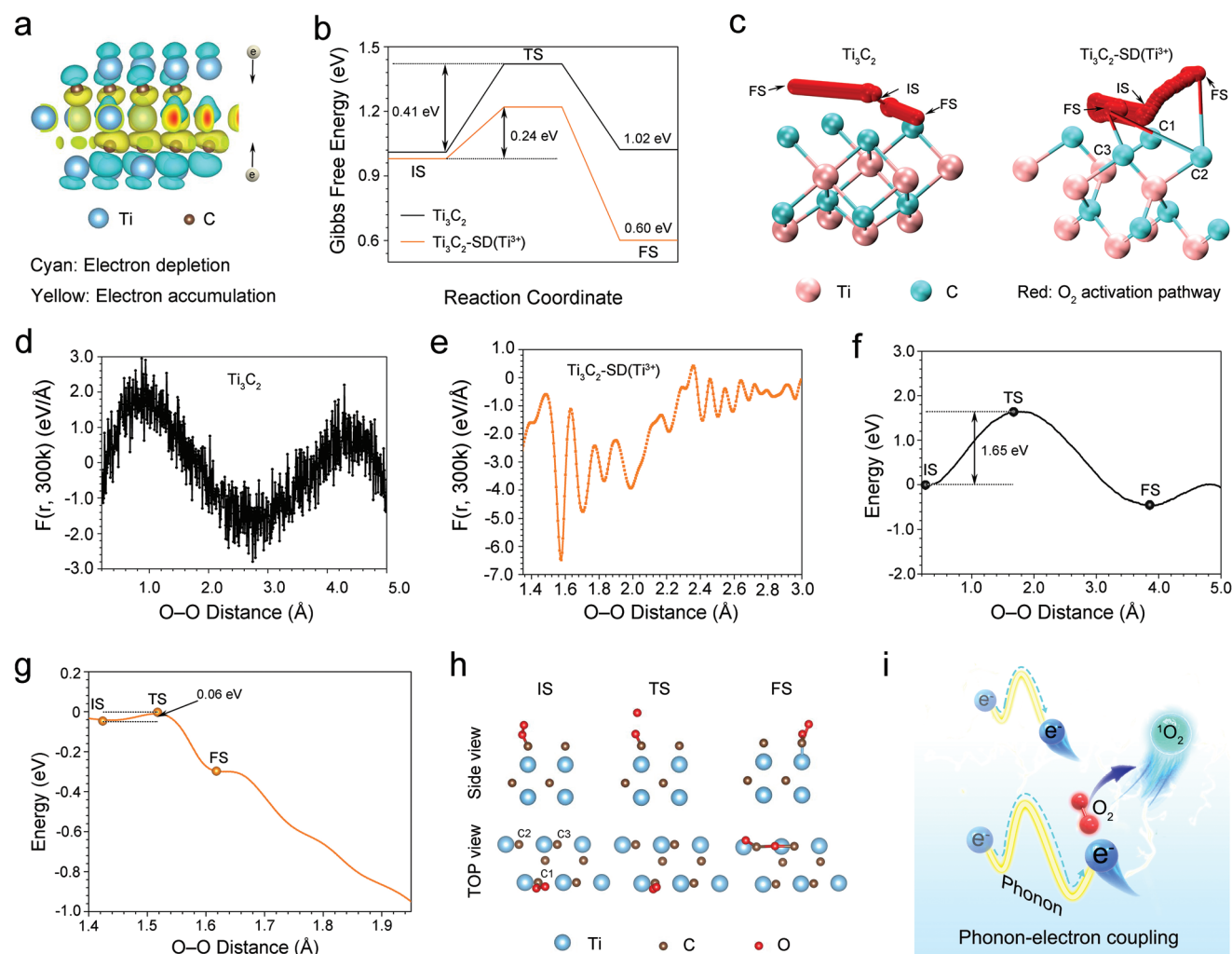


Figure 3. Phonon–electron coupling and O_2 activation on the surface of $\text{Ti}_3\text{C}_2\text{-SD}(\text{Ti}^{3+})$. a) Differential charge density of $\text{Ti}_3\text{C}_2\text{-SD}(\text{Ti}^{3+})$, where cyan and yellow represent electron depletion and accumulation, respectively. b) Gibbs free energy diagram of O_2 activation. IS, TS, and FS correspond to the initial state, transition state, and final state, respectively. The energy difference between IS and TS represents the E_{act} . c) The real O_2 activation pathway (indicated by red) on the surface of pristine Ti_3C_2 (left) and $\text{Ti}_3\text{C}_2\text{-SD}(\text{Ti}^{3+})$ (right). The PMF with increasing distance of O atoms on the surfaces of d) pristine Ti_3C_2 and e) $\text{Ti}_3\text{C}_2\text{-SD}(\text{Ti}^{3+})$. Minimum energy profile of O_2 activation and dissociation process on the surface of f) pristine Ti_3C_2 and g) $\text{Ti}_3\text{C}_2\text{-SD}(\text{Ti}^{3+})$ obtained by integrating the PMF with the entire distance during the separation of the O atoms. h) Representative snapshots of O_2 activation and the dissociation process on the surface of $\text{Ti}_3\text{C}_2\text{-SD}(\text{Ti}^{3+})$. i) Schematic illustration of the phonon–electron coupling effect.

(Figure 3c, indicated by red) and then calculated the potential of mean force (PMF) with increasing distance of O atoms on the surfaces of pristine Ti_3C_2 (Figure 3d) and $\text{Ti}_3\text{C}_2\text{-SD}(\text{Ti}^{3+})$ (Figure 3e). Subsequently, we obtained the energy profile for the reaction by integrating the PMF with the distance during the separation of the O atoms. Here, the E_{act} of pristine Ti_3C_2 for O_2 dramatically increased from 0.41 to 1.65 eV (Figure 3f), indicating that US-triggered lattice vibration inhibited electron transfer, resulting in a higher energy barrier for O_2 activation. In contrast, 2D catalytic planar defects-engineered $\text{Ti}_3\text{C}_2\text{-SD}(\text{Ti}^{3+})$ showed a lower O_2 activation energy barrier (0.06 eV) upon lattice vibration (Figure 3g). We hypothesized that there was a strong coupling effect between the electrons and phonons emitted by US-triggered lattice vibration, facilitating the participation of electrons in O_2 activation and $^1\text{O}_2$ generation.

Finally, we obtained snapshots of three important stages (IS, TS, and FS) in the O_2 activation pathway on the surface of $\text{Ti}_3\text{C}_2\text{-SD}(\text{Ti}^{3+})$ (Figure 3c,h). O_2 was first adsorbed on the C atom (indicated by C1) in the IS stage, which could be attributed to the electron enrichment on the surface of the C atom (Figure 3a). Meanwhile, the rapid electron transfer driven by the phonon–electron coupling effect accelerated O_2 activation and oxygen atom separation in the TS stage.^[41,42] In the FS stage, two oxygen atoms were successfully separated and adsorbed on the other two C atoms (indicated by C2 and C3). Thus, these results evidenced that the phonon–electron coupling effect promoted the REDOX reaction between electrons and O_2 and realized the $^1\text{O}_2$ production.

3.3. Neutrophil Membrane Proteins Coating and Sonodynamic Bactericidal Performance

We then coated NM proteins onto the surface of $\text{Ti}_3\text{C}_2\text{-SD}(\text{Ti}^{3+})$ sheets by electrostatic adsorption to improve their anti-inflammatory capability. In fact, neutrophils have been found to alleviate inflammation owing to their membrane IL-1 receptor (IL-1R) and CD11 antigen-like family member B (CD11b) proteins.^[25,43] Through coating the cell membrane proteins onto the nanomaterials, these cell-mimicking biomaterials inherit the antigenic profile and membrane proteins functions of the source cells.^[44] The surface zeta potential (ζ) result showed that the negatively charged NM and $\text{Ti}_3\text{C}_2\text{-SD}(\text{Ti}^{3+})$ were bridged by the positively charged CS (Figure 4a). The apparent cell membranes (indicated by red arrows) were adsorbed on the $\text{Ti}_3\text{C}_2\text{-SD}(\text{Ti}^{3+})$ sheets from the TEM observation (Figure S7, Supporting Information). Moreover, the hydraulic diameter of the NM-decorated $\text{Ti}_3\text{C}_2\text{-SD}(\text{Ti}^{3+})$ (NM- $\text{Ti}_3\text{C}_2\text{-SD}(\text{Ti}^{3+})$) was about 2–3 μm (Figure S8, Supporting Information), which is consistent with TEM observation. Immunoblotting confirmed the enrichment and presence of key surface proteins, including IL-1R, CD11b, and toll-like receptor 2 (TLR2, recognition of MRSA) on the $\text{Ti}_3\text{C}_2\text{-SD}(\text{Ti}^{3+})$ sheets (Figure 4b)^[25,43,45] in which these results highlighted the feasibility of translocating the NM proteins onto the $\text{Ti}_3\text{C}_2\text{-SD}(\text{Ti}^{3+})$ sheets. In addition, the quantitative analysis verified that about 70% of NM was attached to the $\text{Ti}_3\text{C}_2\text{-SD}(\text{Ti}^{3+})$ (Figure S9, Supporting Information). The NM- $\text{Ti}_3\text{C}_2\text{-SD}(\text{Ti}^{3+})$ exhibited almost the same peak intensity compared with the $\text{Ti}_3\text{C}_2\text{-SD}(\text{Ti}^{3+})$ in $^1\text{O}_2$ detection

(Figure S10, Supporting Information), suggesting that the NM modification would not have a negative effect on the US-triggered $^1\text{O}_2$ generation.

The sonodynamic bactericidal performances of $\text{Ti}_3\text{C}_2\text{-SD}(\text{Ti}^{3+})$ and NM- $\text{Ti}_3\text{C}_2\text{-SD}(\text{Ti}^{3+})$ were then examined. None of the samples demonstrated obvious bactericidal effect in the dark cycle (US (–)), and the corresponding viable colonies of MRSA cells grew well on LB agar plates (Figure S11, Supporting Information). Moreover, the US alone (US (+)) could not inhibit the growth of MRSA colonies at all. However, the colonies of MRSA cells treated with $\text{Ti}_3\text{C}_2\text{-SD}(\text{Ti}^{3+})$ plus US were significantly reduced (Figure S11, Supporting Information), and a corresponding $\approx 2\text{-log}_{10}$ (CFU mL^{-1}) (CFU: colony-forming unit) reduction with the antibacterial ratio of $94.52\% \pm 1.27\%$ was observed (Figure 4c and Figure S12, Supporting Information). The viable colonies and log_{10} (CFU mL^{-1}) were further reduced and the reduction of MRSA count was $99.72\% \pm 0.03\%$, when the MRSA cells were subjected to NM- $\text{Ti}_3\text{C}_2\text{-SD}(\text{Ti}^{3+})$ plus US treatment for 10 min. The in vitro bactericidal performances were subsequently investigated by live/dead dual-color fluorescent staining. All the MRSA cells cultured on the $\text{Ti}_3\text{C}_2\text{-SD}(\text{Ti}^{3+})$, NM- $\text{Ti}_3\text{C}_2\text{-SD}(\text{Ti}^{3+})$, US alone, and the control were able to survive (green) (Figure 4d). In contrast, most of the MRSA cells cultured on the $\text{Ti}_3\text{C}_2\text{-SD}(\text{Ti}^{3+})$ with US treatment were dead (red). The proportion of dead MRSA (red) cells on NM- $\text{Ti}_3\text{C}_2\text{-SD}(\text{Ti}^{3+})$ plus US group was close to 100%, and this result was consistent with that of the spread plate count.

The morphological observation, permeability of the cytoplasmic membrane, oxidative stress, protein leakage, and ATP activity of MRSA cells were further evaluated to unveil its bactericidal mechanism. The SEM results showed that the MRSA cells treated by $\text{Ti}_3\text{C}_2\text{-SD}(\text{Ti}^{3+})$, NM- $\text{Ti}_3\text{C}_2\text{-SD}(\text{Ti}^{3+})$, US alone, and the control presented a typical spherical shape with intact membrane (Figure 4e). However, both $\text{Ti}_3\text{C}_2\text{-SD}(\text{Ti}^{3+})$ and NM- $\text{Ti}_3\text{C}_2\text{-SD}(\text{Ti}^{3+})$ after US treatment induced severe damage to the bacterial membrane integrity, as indicated by red arrows. We further demonstrated that the $\text{Ti}_3\text{C}_2\text{-SD}(\text{Ti}^{3+})$ sheets were unable to capture the MRSA cells as compared with the NM- $\text{Ti}_3\text{C}_2\text{-SD}(\text{Ti}^{3+})$ sheets. FCM analysis was further used to evaluate the adherence to MRSA.^[45] $\text{Ti}_3\text{C}_2\text{-SD}(\text{Ti}^{3+})$ sheets only captured 0.45% MRSA, while NM- $\text{Ti}_3\text{C}_2\text{-SD}(\text{Ti}^{3+})$ sheets acquired a much higher binding rate (10.80%) (Figure 4f), suggesting that the binding rate of our newly developed sheets seems to be better than the others.^[45] The better performance of NM- $\text{Ti}_3\text{C}_2\text{-SD}(\text{Ti}^{3+})$ sheets might correlate to the TLR2 protein (recognition of MRSA) on $\text{Ti}_3\text{C}_2\text{-SD}(\text{Ti}^{3+})$ sheets. Protein coatings are also well known to gain potential antibiofouling effect for a broad spectrum of species including proteins, metabolites, cells, and biofluids under various biological conditions.^[46,47] However, the NM- $\text{Ti}_3\text{C}_2\text{-SD}(\text{Ti}^{3+})$ sheets demonstrated an ability to capture MRSA, possibly because of the specific TLR2 protein in NM that may help recognize and target MRSA. Obviously, this targeted approach with NM coating could enhance the antibacterial efficiency of $\text{Ti}_3\text{C}_2\text{-SD}(\text{Ti}^{3+})$. Next, ONPG was used to study the cytoplasmic membrane permeability, in which a higher ONPG intensity suggested a stronger membrane permeability. The highest ONPG intensity was observed in the NM- $\text{Ti}_3\text{C}_2\text{-SD}(\text{Ti}^{3+})$ group (Figure 4g), indicating that NM- $\text{Ti}_3\text{C}_2\text{-SD}(\text{Ti}^{3+})$ plus US treatment effectively promoted the

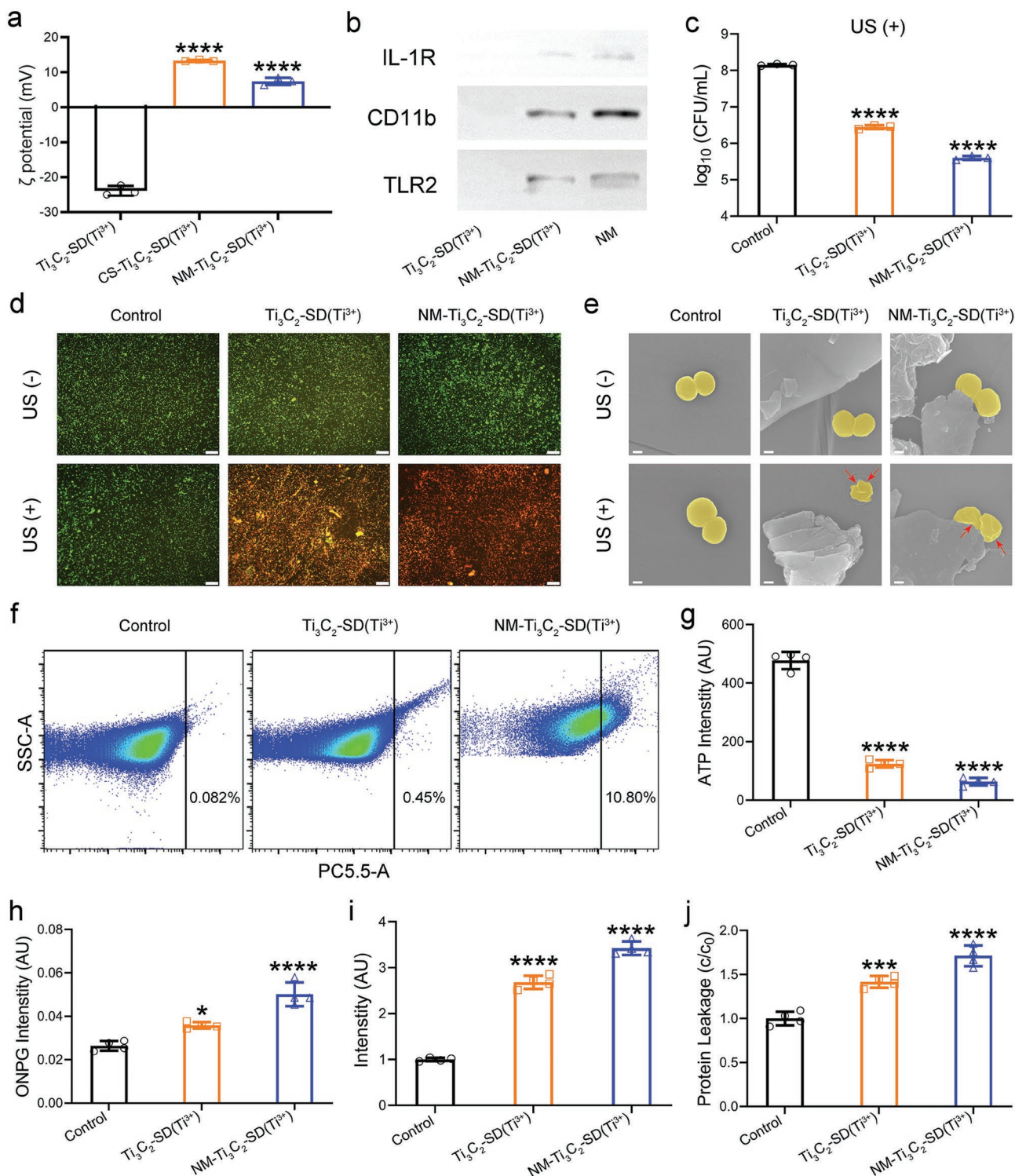


Figure 4. Sonodynamic bactericidal performance of $\text{NM-Ti}_3\text{C}_2\text{-SD}(\text{Ti}^{3+})$. a) Surface ζ -potential of $\text{Ti}_3\text{C}_2\text{-SD}(\text{Ti}^{3+})$, $\text{CS-Ti}_3\text{C}_2\text{-SD}(\text{Ti}^{3+})$, and $\text{NM-Ti}_3\text{C}_2\text{-SD}(\text{Ti}^{3+})$. b) Characteristic protein bands of $\text{Ti}_3\text{C}_2\text{-SD}(\text{Ti}^{3+})$, $\text{NM-Ti}_3\text{C}_2\text{-SD}(\text{Ti}^{3+})$, and NM resolved by western blotting. c) MRSA-killing abilities of different samples after treatment with US (US (+)) for 10 min. d) Fluorescent images of live (green) and dead (red) MRSA after treatment by different samples without (US (-)) or with (US (+)) US for 10 min. Scale bars: 50 μm . e) SEM images of MRSA on different samples without (US (-)) or with (US (+)) US for 10 min treatment. Red arrows denote morphological damage in MRSA. Scale bars: 200 nm. f) The adherence of $\text{Ti}_3\text{C}_2\text{-SD}(\text{Ti}^{3+})$ and $\text{NM-Ti}_3\text{C}_2\text{-SD}(\text{Ti}^{3+})$ to MRSA by flow cytometry. g) ATP activity, h) Cytoplasmic membrane permeability, i) oxidative stress, and j) protein leakage of MRSA after treatment with different samples with US for 10 min. Data were obtained from independent samples ($n = 3$ for [a]–[c], while $n = 4$ for [f]–[j]). The error bars indicate mean \pm standard deviations: * $p < 0.05$, ** $p < 0.01$, *** $p < 0.001$, and **** $p < 0.0001$; ns: not significant ($p > 0.05$). The statistical analysis was performed using one-way analysis of variance with the Tukey multiple-comparisons test.

cytoplasmic membrane permeability of MRSA cells. The subsequent changes detected in the cytoplasm of MRSA cells might further unveil the bactericidal mechanism. Higher fluorescence intensity detected by the ROS Assay Kit indicated increased oxidative stress. The NM-Ti₃C₂-SD(Ti³⁺) group demonstrated the strongest fluorescence intensity (Figure 4h), suggesting that NM-Ti₃C₂-SD(Ti³⁺) plus US treatment induced intensive oxidative stress in MRSA cells owing to tremendous ¹O₂ generation. It also significantly induced protein leakage (Figure 4i) and decreased ATP activity (Figure 4j) in MRSA cells. The NM-Ti₃C₂-SD(Ti³⁺) also demonstrated the powerful disruption ability against the MRSA biofilm (indicated by blue arrows) due to the effective release of US-triggered ¹O₂ and targeted bacterial capture (Figure S13, Supporting Information).

3.4. Regulation of Macrophage and Bone Marrow Mesenchymal Stem Cells

Macrophage-mediated immunoregulation is essential for inflammatory tissue response and the subsequent expression of pro-healing cytokines in bony tissue.^[48] Therefore, we next investigated the gene expression profile of macrophages induced by NM-Ti₃C₂-SD(Ti³⁺) sheets in vitro. First, the MTT assay revealed that both Ti₃C₂-SD(Ti³⁺) and NM-Ti₃C₂-SD(Ti³⁺) sheets presented good biocompatibility to macrophages (Figure S14, Supporting Information). The qRT-PCR and ELISA were applied to detect the genes expressions induced by M1 phenotype macrophages (i.e., iNOS, C-C chemokine receptor type 7 [CCR7], and TNF- α) and the release of corresponding pro-inflammatory cytokines,^[49,50] and the anti-inflammatory cytokines expressed by M2 phenotype macrophages,^[51,52] including arginase-1 (Arg-1), mannose receptor CD206, and interleukin-10 (IL-10), respectively. The results showed that the mRNA expressions of the M1 markers (iNOS, CCR7, and TNF- α) were upregulated in macrophages after incubating with sheets for 1 day, while the mRNA expressions of M2 markers (Arg-1, CD206, and IL-10) were downregulated (Figure 5a and Figure S15, Supporting Information). This observation may be attributed to the chemotaxis of macrophages in response to foreign body invasion.^[53] After 3 days, the macrophages cultured with Ti₃C₂-SD(Ti³⁺) sheets still expressed high mRNA levels of pro-inflammatory M1 markers (Figure 5b and Figure S16a, Supporting Information), whereas the NM-Ti₃C₂-SD(Ti³⁺) sheets could significantly upregulate the mRNA expression of anti-inflammatory markers because of the polarization of macrophages toward M2 (Figure 5b and Figure S16b, Supporting Information). The ELISA result further suggested that the levels of pro-inflammatory cytokines (TNF- α and iNOS) were elevated in both Ti₃C₂-SD(Ti³⁺) and NM-Ti₃C₂-SD(Ti³⁺) groups at the early stage (Figure 5c and Figure S17a, Supporting Information), whereas the expressions of anti-inflammatory cytokines (IL-10 and Arg-1) among all groups made no significant difference at all (Figure 5d and Figure S17b, Supporting Information). When comparing the results obtained from long-term incubation, the NM-modified sheets significantly inhibited the secretion of pro-inflammatory cytokines in macrophages (Figure 5e and Figure S17a, Supporting Information). Moreover, the NM-Ti₃C₂-SD(Ti³⁺) sheets could also convince macrophages to secrete a

large number of anti-inflammatory cytokines (Figure 5f and Figure S17b, Supporting Information). We further evaluated ROS-induced inflammatory response by 10 min of US treatment after co-cultured the macrophages with the sheets. After 1 day, the synergistic reaction of the foreign body invasion and ROS induced severe inflammatory response in both Ti₃C₂-SD(Ti³⁺) and NM-Ti₃C₂-SD(Ti³⁺) groups (Figure S18a,b, Supporting Information). Ti₃C₂-SD(Ti³⁺) sheets still expressed high mRNA levels of pro-inflammatory marker (TNF- α) after long-term incubation. However, the NM-modified sheets significantly upregulated the mRNA expression of anti-inflammatory marker (IL-10) (Figure S18c,d, Supporting Information).

In addition, the results of fluorescent images and MTT assays showed that both Ti₃C₂-SD(Ti³⁺) and NM-Ti₃C₂-SD(Ti³⁺) sheets could also facilitate the proliferation of BMSCs (Figure 5g). Furthermore, the results of qRT-PCR suggested that both Ti₃C₂-SD(Ti³⁺) and NM-Ti₃C₂-SD(Ti³⁺) sheets substantially promoted the mRNA expressions of the osteogenesis-related genes, including *Alkaline phosphatase (ALP)*, *Osterix (OSX)*, *Runt-related transcription factor 2 (Runx-2)*, and its downstream osteogenic genes *Collagen type I (COL I)*, *Osteocalcin (OCN)*, and *Osteopontin (OPN)* (Figure 5h and Figure S19, Supporting Information). Also, neither Ti₃C₂-SD(Ti³⁺) nor NM-Ti₃C₂-SD(Ti³⁺) sheets would cause the lysis of RBCs according to the haemolysis testing results (Figure S20, Supporting Information).

Sonosensitizers and their related SDT are commonly used in antibacterial and tumor therapies, particularly in those related to deep-seated tissues.^[54–56] Most sonosensitizers rarely consider the issue of biocompatibility. For example, purpurin 18 and protoporphyrin IX can effectively remove MRSA infection from muscle and/or subcutaneous solid tumors, respectively. However, the anti-inflammatory and tissue repair capabilities of purpurin 18 and protoporphyrin IX have not been thoroughly addressed.^[54,55] In particular, protoporphyrin IX exhibited significant cytotoxicity when the concentration reached to 200 $\mu\text{g mL}^{-1}$ (Figure S21, Supporting Information), suggesting that its biosafety would become a concern. In contrast, when our Ti₃C₂-SD(Ti³⁺) sheets decorated with NM proteins adopted, they demonstrated a high degree of cell proliferation and differentiation, even though the concentration was about 500 $\mu\text{g mL}^{-1}$. Furthermore, our newly developed sonosensitizers can effectively suppress tissue inflammation. These evidences show that the NM-Ti₃C₂-SD(Ti³⁺) sheets can properly address osteogenic ability, biosafety, and anti-inflammatory issues when considered for clinical application.

3.5. Pre-Clinical Evaluation in the Bony Tissue Infection Animal Model

Since bony tissue infection is one of the highest deep-seated infections risks,^[57,58] we challenged the SDT efficacy of our newly developed sonosensitizer by using mouse models infected with MRSA cells on bony tissue. The MRSA cells were first injected into bone marrow through a defect (0.5 mm in diameter) on the tibia to establish a bone infection model. After 1 day, the bone tissue was collected for the plate counting experiment. Compared to normal bone tissue, a large number of viable colonies of MRSA cells grew well on

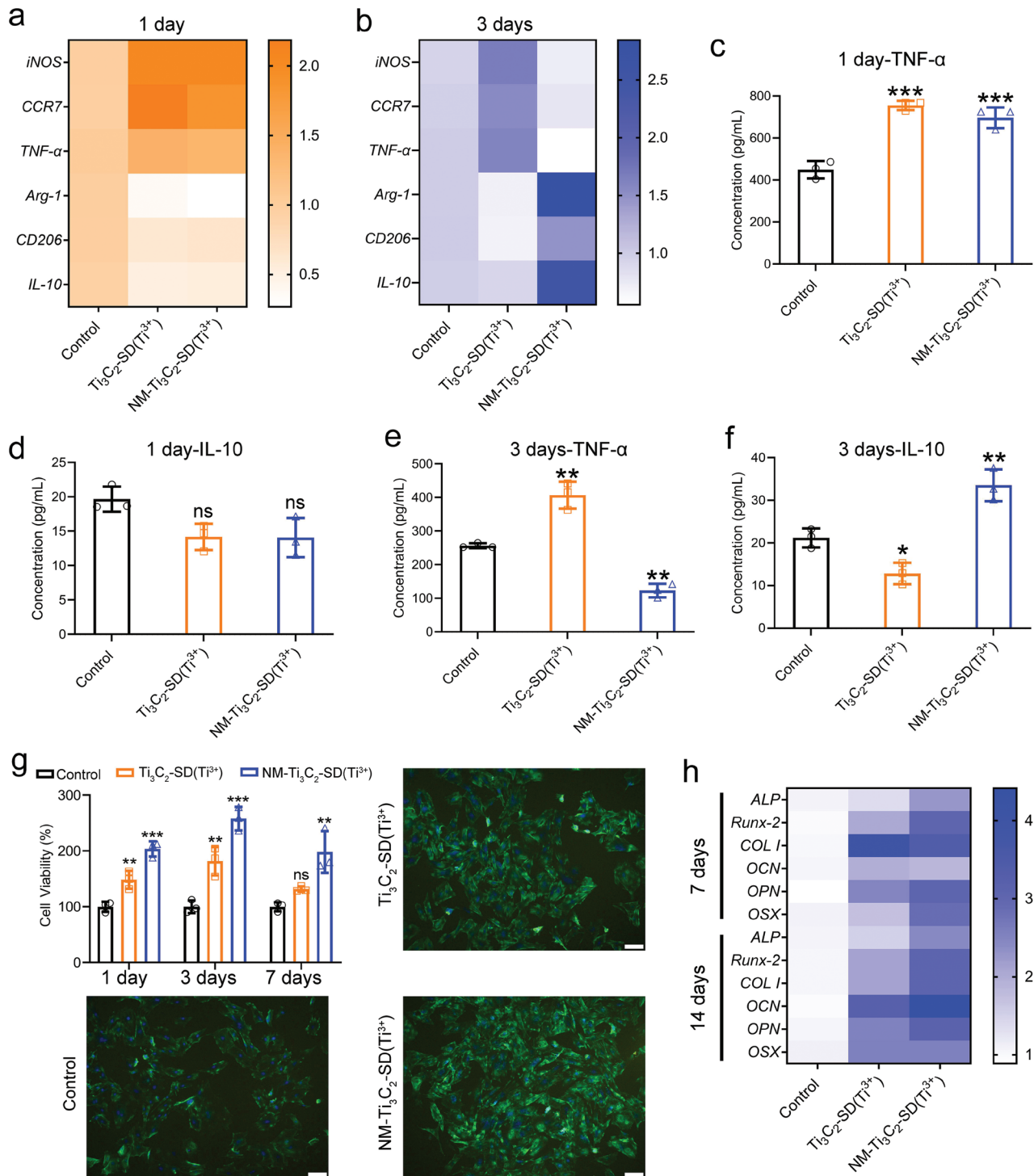


Figure 5. Inflammatory response and osteogenic capability of NM-Ti₃C₂-SD(Ti³⁺). a,b) Heat maps of the M1 macrophage genes (i.e., *inducible nitric oxide synthase* [iNOS], *C-C chemokine receptor type 7* [CCR7], and *tumor necrosis factor-alpha* [TNF-α]), the expression level and M2 macrophage genes (i.e., *arginase-1* [Arg-1], *mannose receptor CD206*, and *interleukin-10* [IL-10]), and the expression level in macrophages after being co-cultured with different samples for a) 1 and b) 3 days. The secretion of c) TNF-α and d) IL-10 from macrophages after being co-cultured with different samples for 1 day. The secretion of e) TNF-α and f) IL-10 from macrophages after being co-cultured with different samples for 3 days. g) The cell viability of bone marrow mesenchymal stem cells (BMSCs) after being co-cultured with different samples for 1, 3, and 7 days and corresponding fluorescent images of 1 day. Scale bars: 50 μm. h) Heat map of the mRNA expressions of osteogenesis-related genes of BMSCs after co-culture with different samples for 7 and 14 days. The color bar in the heat maps indicates the multiples of gene regulation, where darker color indicates higher gene upregulation. Data were obtained from independent samples ($n = 3$). The error bars indicate mean \pm standard deviations: * $p < 0.05$, ** $p < 0.01$, *** $p < 0.001$, and **** $p < 0.0001$. The statistical analysis was performed using one-way analysis of variance with the Tukey multiple-comparisons test.

LB agar plates in the model group (Figure S22, Supporting Information), suggesting that the bony tissue infection animal model was successfully established. After 14 days of different

treatments, we still observed the formation of prominent yellowish pus (indicated by red arrows) in both the saline (control) and Ti_3C_2 -SD(Ti^{3+}) groups (Figure 6a), indicating that

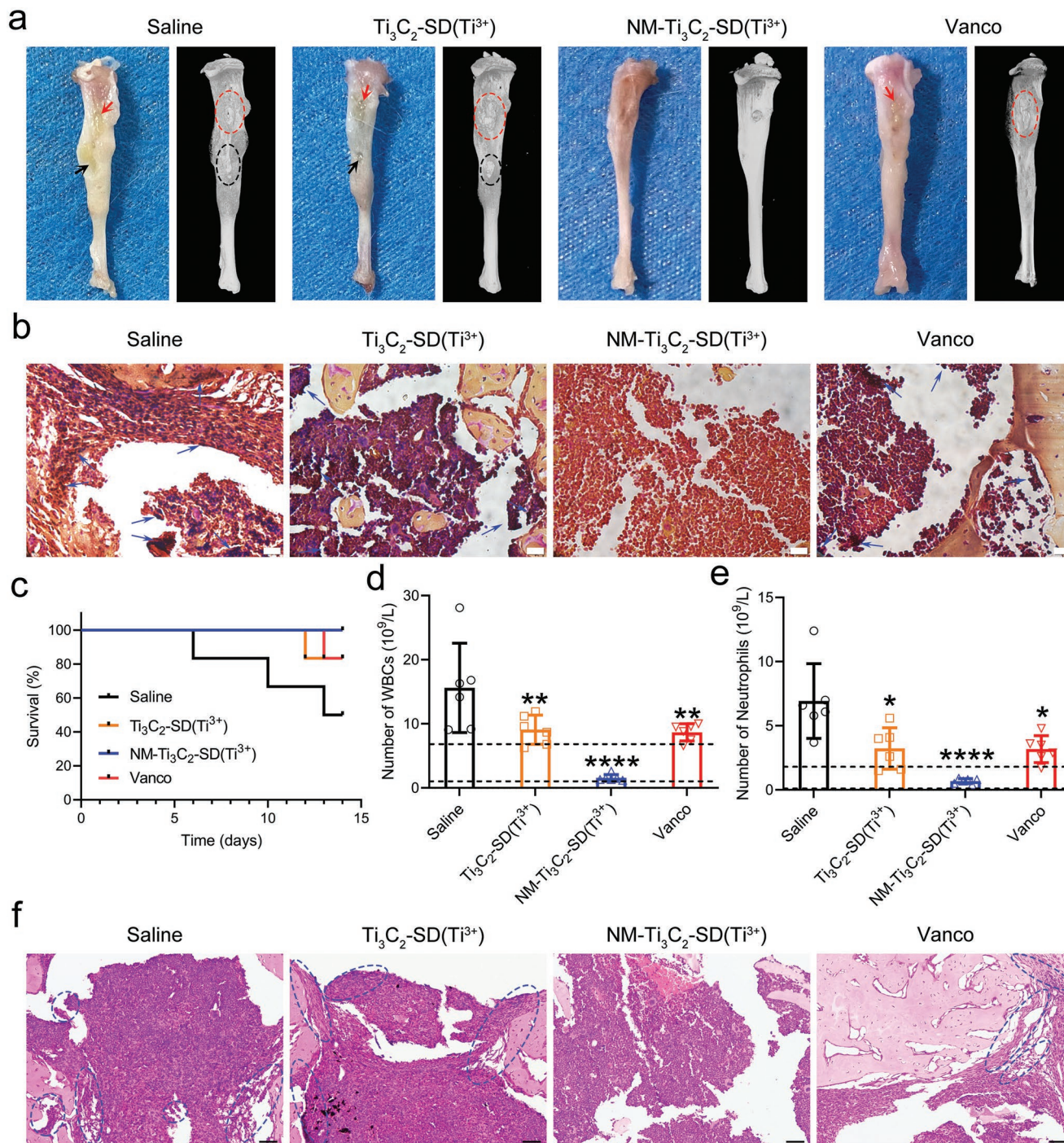


Figure 6. Sonodynamic bactericidal performance of NM- Ti_3C_2 -SD(Ti^{3+}) in MRSA-infected bony tissue in vivo. a) Macroscopic images of infected tibia specimens of mice after 14 days of different treatments. Red arrows: yellowish pus at the site of bone defects; black arrows: suppuration on the distal tibias; red dashed ellipse: bone destruction at the site of bone defects; black dashed ellipses: bone destruction on the distal tibias. b) Gram staining images of infected bony tissue after 14 days of different treatments. Blue arrows: dark purple crystal remains of MRSA. Scale bars: 20 μm . c) Survival rate ($n = 6$) of MRSA-infected mice after different treatments. The number of d) WBCs and e) neutrophils in the blood of MRSA-infected mice after 14 days of different treatments. Data were obtained from independent samples ($n = 6$). The error bars indicate mean \pm standard deviations: * $p < 0.05$, ** $p < 0.01$, *** $p < 0.001$, and **** $p < 0.0001$. The statistical analysis was performed using one-way analysis of variance with the Tukey multiple-comparisons test. f) H&E staining images of infected bony tissues after 14 days of different treatments. Blue dashed ellipse: inflammatory cells. Scale bars: 50 μm .

severe MRSA bacterial infection was found. The results of μ -CT images highlighted that the bone defects in both the control and $\text{Ti}_3\text{C}_2\text{-SD}(\text{Ti}^{3+})$ groups were enlarged (indicated by red dashed ellipses) due to serious bacterial infections. We also observed significant suppuration (indicated by black arrows) and bony destruction on the distal tibias (indicated by black dashed ellipses) that led to severe bone deformity in these two groups.

In contrast, the tibia specimen collected from the NM- $\text{Ti}_3\text{C}_2\text{-SD}(\text{Ti}^{3+})$ group presented no abnormalities, apparent festering, or bone damage, demonstrating that the modified NM sheets combined with US treatment could effectively combat MRSA bacterial infection on bone. Unexpectedly, the vancomycin (Vanco) treatment was unable to address pus formation (indicated by red arrow) or bone destruction (indicated by red dashed ellipse) at the bone defect infected with MRSA cells. We then performed the plate counting experiment on the harvested bony tissues after various treatments for 14 days to quantify the antibacterial property of NM- $\text{Ti}_3\text{C}_2\text{-SD}(\text{Ti}^{3+})$. All the treatment groups showed a reduction of MRSA bacterial colonies. Of these, the NM- $\text{Ti}_3\text{C}_2\text{-SD}(\text{Ti}^{3+})$ group exhibited a 6- \log_{10} reduction in MRSA bacterial burden in the bony tissue after 14 days of treatment and demonstrated the highest antibacterial efficacy against MRSA in vivo (Figure S23, Supporting Information). In fact, intracellular infection, osteocyte lacunacanalicular network invasion, biofilm formation, and abscess formation can contribute to long-term bacterial persistence and immune evasion, thus leading to the failure of antibiotic treatment in MRSA cell-induced bony tissue infection and osteomyelitis.^[53,59] Additionally, we used Gram staining to further evaluate residual bacteria in bony tissue.^[60] A large number of dark purple spots (indicated by blue arrows, Figure 6b) were observed in the bony tissue of the other treatment groups, whereas the NM- $\text{Ti}_3\text{C}_2\text{-SD}(\text{Ti}^{3+})$ group was relatively “clean.” This suggests that the MRSA bacterial residues were still found in the marrow cavity, which was consistently observed from the macroscopic images.

MRSA-induced bony tissue infection is a clinically life-threatening disease,^[61] we therefore further documented the mortality rate during the entire treatment process. There were death cases after 6 days of treatment and the mortality rate increased to as high as 50% after 14 days in the saline group (Figure 6c). There were 16.7% of mice dead in both $\text{Ti}_3\text{C}_2\text{-SD}(\text{Ti}^{3+})$ plus US and Vanco groups after 14 days of treatment, which was comparable to clinical mortality (15–17%) by conventional antibiotic treatment.^[61] As expected, there was no death found in the NM- $\text{Ti}_3\text{C}_2\text{-SD}(\text{Ti}^{3+})$ plus US group over the course of treatment, which likely benefited from the robust antibacterial efficiency of the NM- $\text{Ti}_3\text{C}_2\text{-SD}(\text{Ti}^{3+})$ sheets.

Bacterial infection inevitably causes an inflammatory response in the host. We therefore analyzed inflammation in the mouse models by routine blood examination. White blood cells (WBCs) and neutrophils are typical inflammation markers used to screen for the severity of bacterial infection.^[62] Compared with the NM- $\text{Ti}_3\text{C}_2\text{-SD}(\text{Ti}^{3+})$ group, the numbers of WBCs (Figure 6d) and neutrophils (Figure 6e) in the other three groups, especially in the saline group, were significantly higher than the normal range (indicated by two black dashed lines), suggesting that the inflammatory response caused by

MRSA infection was obvious. Similarly, hematoxylin and eosin (H&E) staining at day 14 showed numerous inflammatory cells (indicated by blue dashed ellipses) in the bony tissues of saline, $\text{Ti}_3\text{C}_2\text{-SD}(\text{Ti}^{3+})$, and Vanco groups owing to severe MRSA infection and inflammation (Figure 6f). In contrast, there was negligible inflammatory response in both blood and bony tissues of NM- $\text{Ti}_3\text{C}_2\text{-SD}(\text{Ti}^{3+})$ group.

We also evaluated the inflammatory response in bony tissue and the anti-inflammatory efficacy of each treatment group using immunofluorescence. The results of immunofluorescent staining on bony tissue sections revealed that the expressions of $\text{TNF-}\alpha$ (Figure 7a,b) and iNOS (Figure S24, Supporting Information) in the NM- $\text{Ti}_3\text{C}_2\text{-SD}(\text{Ti}^{3+})$ group were lowest among all treatment groups. This demonstrated that the modified sheets combined with US intervention induced a minimal tissue inflammation response. Furthermore, the bony tissue section obtained from the NM- $\text{Ti}_3\text{C}_2\text{-SD}(\text{Ti}^{3+})$ group expressed the highest level of IL-10 (Figure 7c,d) and Arg-1 (Figure S25, Supporting Information), highlighting that macrophage polarization toward the M2 phenotype was induced by NM- $\text{Ti}_3\text{C}_2\text{-SD}(\text{Ti}^{3+})$ sheets, which contributed to the anti-inflammatory effect.

The bony tissue sections with immunofluorescent staining further revealed that the relative expressions of Runx-2 (Figure 7e,f), COL I (Figure 7g,h), and OPN (Figure S26, Supporting Information) in the NM- $\text{Ti}_3\text{C}_2\text{-SD}(\text{Ti}^{3+})$ group were significantly higher than other groups, suggesting that the $\text{Ti}_3\text{C}_2\text{-SD}(\text{Ti}^{3+})$ -based sheets could even promote bone growth after MRSA infection was eradicated in vivo. We also analyzed the harvested bone tissues based on the longitudinal sections (indicated by the light blue areas) of the 3D reconstructed μ -CT images (Figure 7i). Severe bone destruction and bone loss were observed in the control (saline), $\text{Ti}_3\text{C}_2\text{-SD}(\text{Ti}^{3+})$, and Vanco groups (Figure 7i), whereas healthy bone tissue with high bone density was found on the NM- $\text{Ti}_3\text{C}_2\text{-SD}(\text{Ti}^{3+})$ group. Interestingly, a new bone formation was also identified in the bone defect (indicated by red arrows) (Figure 7i and Figure S27, Supporting Information), which further evidenced the superior osteogenic ability of NM- $\text{Ti}_3\text{C}_2\text{-SD}(\text{Ti}^{3+})$ sheets. The results of H&E staining did not exhibit any acute biotoxicity on the major organs harvested in any of the groups after 14 days of treatment (Figure S28, Supporting Information).

The literature has reported that TiO_2 is a typical sonosensitizer comprising 0D oxygen defects (Table S2, Supporting Information).^[5,34] However, these engineered TiO_2 coatings might not be able to realize a superior antibacterial capability upon US stimulation due to the insufficient ROS generated from oxygen point defects.^[34] To achieve a better antibacterial efficiency, such Schottky point defect-mediated SDT would require additional interventions, such as photothermal therapy and chemodynamic therapy (Table S2, Supporting Information).^[5,16,34] Indeed, our results suggested that the NM- $\text{Ti}_3\text{C}_2\text{-SD}(\text{Ti}^{3+})$ can release a sufficient amount of ROS under US stimulation due to its 2D catalytic planar defects and therefore the MRSA cells engulfed in bony tissue can be substantially reduced. Furthermore, the NM- $\text{Ti}_3\text{C}_2\text{-SD}(\text{Ti}^{3+})$ can also alleviate tissue inflammation and assist bone repair once bony tissue infection has been controlled. All these evidences suggested

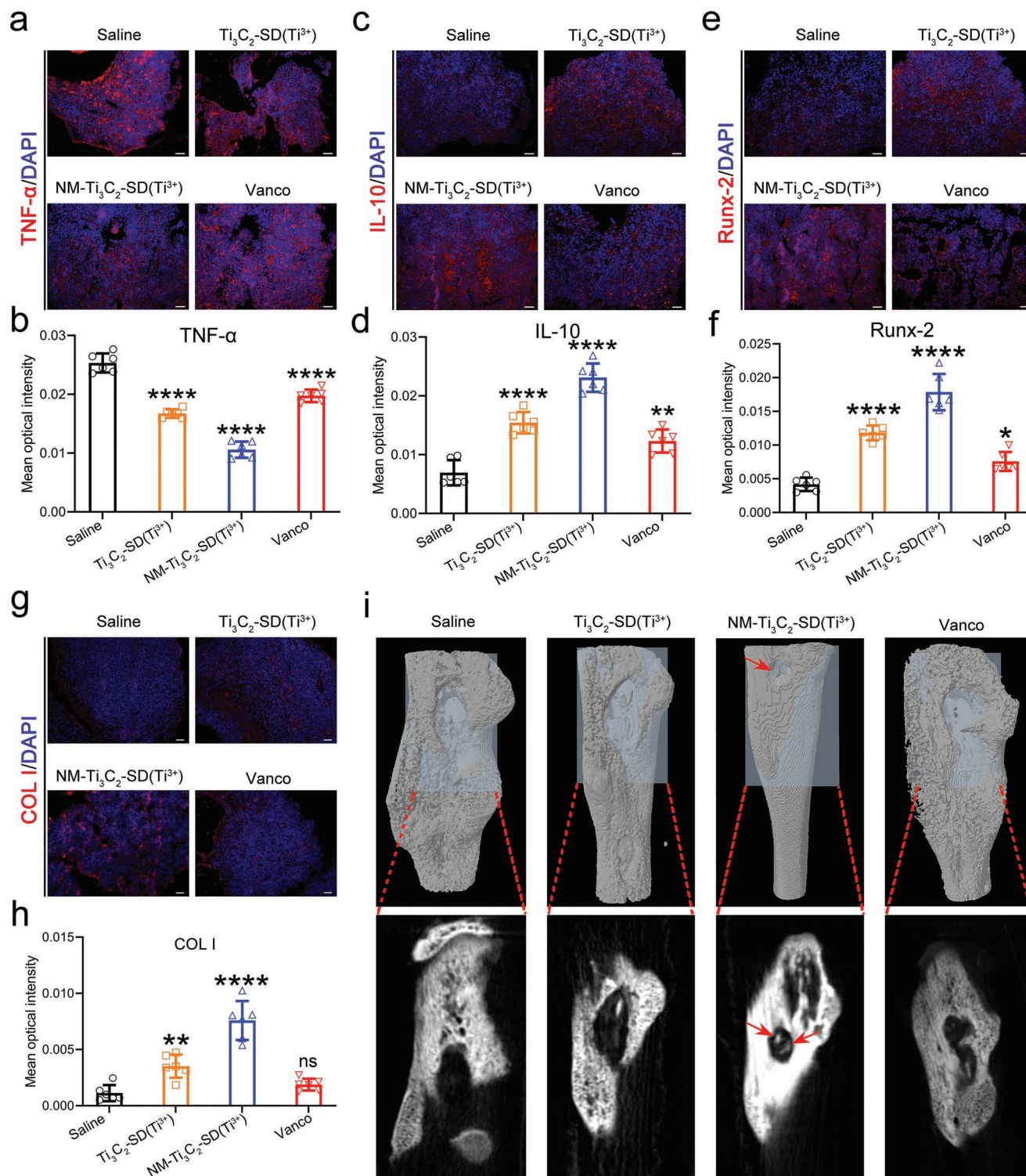


Figure 7. Inflammatory response and bone repair ability in MRSA-infected bony tissue in vivo. The fluorescent images of a) tumor necrosis factor- α (TNF- α), c) interleukin-10 (IL-10), e) Runt-related transcription factor 2 (Runx-2), g) Collagen type I (COL I) and the corresponding mean optical intensity of b) TNF- α , d) IL-10, f) Runx-2, and h) COL I in the MRSA-infected bony tissues after treated with different samples for 14 days. The higher mean optical intensity indicates the more expression of the related proteins. Scale bars: 20 μ m. Data were taken from independent samples ($n = 6$). The error bars indicate mean \pm standard deviation: * $p < 0.05$, ** $p < 0.01$, *** $p < 0.001$, and **** $p < 0.0001$; ns: not significant ($p > 0.05$). The statistical analysis was performed using one-way analysis of variance with the Tukey multiple-comparisons test. i) 3D reconstruction (top) and extracted μ -CT images of the corresponding sections (bottom, indicated by the light blue areas) of harvested bone tissues after treated with different samples for 14 days.

that the modified Ti_3C_2 sheets with 2D catalytic planar defects combined with US intervention are an effective antibacterial strategy to potentially address the complications of bony tissue infection induced by MRSA cells clinically.

4. Conclusion

In summary, we have successfully developed a new sonosensitizer ($\text{Ti}_3\text{C}_2\text{-SD}(\text{Ti}^{3+})$) by conferring 2D catalytic planar defects comprised of slip dislocation with abundant Ti^{3+} species in Ti_3C_2 sheets. The subsequent NM proteins modification ($\text{NM-Ti}_3\text{C}_2\text{-SD}(\text{Ti}^{3+})$) enables efficient elimination of MRSA-induced infection and mitigation of the inflammatory response in bony tissue through the integration of the advantages of SDT and immunoregulation. Through AIMD analysis, our synergistic experimental–theoretical work demonstrates a unique and hitherto unknown SDT mechanism in the 2D catalytic planar defects-engineered sonosensitizer. The phonons emitted from the 2D catalytic planar defects were strongly coupled with the electrons and accelerated the electron transfer to participate in the REDOX reaction and $^1\text{O}_2$ generation. The treatment efficacy of $\text{NM-Ti}_3\text{C}_2\text{-SD}(\text{Ti}^{3+})$ on bony tissue infection far outperformed that of traditional antibiotics owing to its high efficiency of $^1\text{O}_2$ release and targeted therapy on MRSA bacteria. Furthermore, the $\text{NM-Ti}_3\text{C}_2\text{-SD}(\text{Ti}^{3+})$ sheets do not demonstrate any acute bio-safety issues that could jeopardize their clinical feasibility.

Supporting Information

Supporting Information is available from the Wiley Online Library or from the author.

Acknowledgements

This work was jointly supported by National Key R&D Program of China (2018YFA0703100), General Research Fund of Hong Kong Research Grant Council (nos. 17207719 and 17214516), Hong Kong Health and Medical Research Fund (nos. 19180712, 20190422, and 21200592), Innovation and Technology Fund Partnership Research Program (PRP/O30/30FX), Collaborative Research Fund of Hong Kong Research Grant Council (no. C5044-21G), the National Science Fund for Distinguished Youth Scholar (no. 51925104), Shenzhen Science and Technology Funding (nos. JCYJ20210324120012034 and JCYJ20210324120009026), Sanming Project of Medicine in Shenzhen “Team of Excellence in Spinal Deformities and Spinal Degeneration” (SZSM201612055), and HKU-SZH Fund for Shenzhen Key Medical Discipline (SZXK2020084).

Conflict of Interest

The authors declare no conflict of interest.

Data Availability Statement

The data that support the findings of this study are available from the corresponding author upon reasonable request.

Keywords

activation energy, phonon–electron coupling, Schottky defects, sonodynamic therapy, two-dimensional catalytic planar defects

Received: September 21, 2022

Revised: December 11, 2022

Published online:

- [1] Y. Meng, K. Hynynen, N. Lipsman, *Nat. Rev. Neurol.* **2021**, *17*, 7.
- [2] L. Wang, G. Z. Li, L. Cao, Y. Dong, Y. Wang, S. S. Wang, Y. Q. Li, X. H. Guo, Y. Zhang, F. F. Sun, X. M. Du, J. A. Su, Q. Li, X. J. Peng, K. Shao, W. J. Zhao, *Sci. Adv.* **2021**, *7*, eabj4796.
- [3] F. Gong, L. Cheng, N. Yang, Y. Gong, Y. Ni, S. Bai, X. Wang, M. Chen, Q. Chen, Z. Liu, *Nat. Commun.* **2020**, *11*, 3712.
- [4] C. Mao, Y. Xiang, X. Liu, Z. Cui, X. Yang, K. W. K. Yeung, H. Pan, X. Wang, P. K. Chu, S. Wu, *ACS Nano* **2017**, *11*, 9010.
- [5] X. Wang, X. Zhong, L. Bai, J. Xu, F. Gong, Z. Dong, Z. Yang, Z. Zeng, Z. Liu, L. Cheng, *J. Am. Chem. Soc.* **2020**, *142*, 6527.
- [6] Z. Huang, H. Moseley, S. Bown, *Integr. Cancer Ther.* **2010**, *9*, 317.
- [7] T. Inui, K. Makita, H. Miura, A. Matsuda, D. Kuchiike, K. Kubo, M. Mette, Y. Uto, T. Nishikata, H. Hori, N. Sakamoto, *Anticancer Res.* **2014**, *34*, 4589.
- [8] P. Zhu, Y. Chen, J. Shi, *ACS Nano* **2018**, *12*, 3780.
- [9] P. Huang, X. Qian, Y. Chen, L. Yu, H. Lin, L. Wang, Y. Zhu, J. Shi, *J. Am. Chem. Soc.* **2017**, *139*, 1275.
- [10] F. Gong, L. Cheng, N. Yang, O. Betzer, L. Feng, Q. Zhou, Y. Li, R. Chen, R. Popovtzer, Z. Liu, *Adv. Mater.* **2019**, *31*, 1900730.
- [11] X. Wang, X. Zhong, F. Gong, Y. Chao, L. Cheng, *Mater. Horiz.* **2020**, *7*, 2028.
- [12] X. Qian, Y. Zheng, Y. Chen, *Adv. Mater.* **2016**, *28*, 8097.
- [13] S. Son, J. H. Kim, X. Wang, C. Zhang, S. A. Yoon, J. Shin, A. Sharma, M. H. Lee, L. Cheng, J. Wu, J. S. Kim, *Chem. Soc. Rev.* **2020**, *49*, 3244.
- [14] M. Murdoch, G. I. Waterhouse, M. A. Nadeem, J. B. Metson, M. A. Keane, R. F. Howe, J. Llorca, H. Idriss, *Nat. Chem.* **2011**, *3*, 489.
- [15] V. G. Deepagan, D. G. You, W. Um, H. Ko, S. Kwon, K. Y. Choi, G. R. Yi, J. Y. Lee, D. S. Lee, K. Kim, I. C. Kwon, J. H. Park, *Nano Lett.* **2016**, *16*, 6257.
- [16] S. Liang, X. Xiao, L. Bai, B. Liu, M. Yuan, P. Ma, M. Pang, Z. Cheng, J. Lin, *Adv. Mater.* **2021**, *33*, 2100333.
- [17] J. S. Park, S. Kim, Z. Xie, A. Walsh, *Nat. Rev. Mater.* **2018**, *3*, 194.
- [18] X. B. Chen, L. Liu, P. Y. Yu, S. S. Mao, *Science* **2011**, *331*, 746.
- [19] Y. Zhang, X. Zhang, H. Yang, L. Yu, Y. Xu, A. Sharma, P. Yin, X. Li, J. S. Kim, Y. Sun, *Chem. Soc. Rev.* **2021**, *50*, 11227.
- [20] M. A. Rajora, J. W. H. Lou, G. Zheng, *Chem. Soc. Rev.* **2017**, *46*, 6433.
- [21] Y. Zhu, D. D. Liu, H. J. Jing, F. Zhang, X. B. Zhang, S. Q. Hu, L. M. Zhang, J. Y. Wang, L. X. Zhang, W. H. Zhang, B. J. Pang, P. Zhang, F. T. Fan, J. P. Xiao, W. Liu, X. F. Zhu, W. S. Yang, *Sci. Adv.* **2022**, *8*, eabn4072.
- [22] H. Wang, X. Liu, X. Yan, J. Fan, D. Li, J. Ren, X. Qu, *Chem. Sci.* **2022**, *13*, 6704.
- [23] M. Zhang, D. Yang, C. Dong, H. Huang, G. Feng, Q. Chen, Y. Zheng, H. Tang, Y. Chen, X. Jing, *ACS Nano* **2022**, *16*, 9938.
- [24] A. Sarycheva, A. Polemi, Y. L. Liu, K. Dandekar, B. Anasori, Y. Gogotsi, *Sci. Adv.* **2018**, *4*, eaau0920.
- [25] Q. Zhang, D. Dehaini, Y. Zhang, J. Zhou, X. Chen, L. Zhang, R. H. Fang, W. Gao, L. Zhang, *Nat. Nanotechnol.* **2018**, *13*, 1182.
- [26] L. Tan, J. Li, X. Liu, Z. Cui, X. Yang, S. Zhu, Z. Li, X. Yuan, Y. Zheng, K. W. K. Yeung, H. Pan, X. Wang, S. Wu, *Adv. Mater.* **2018**, *30*, 1801808.

- [27] V. Kamysbayev, A. S. Filatov, H. C. Hu, X. Rui, F. Lagunas, D. Wang, R. F. Klie, D. V. Talapin, *Science* **2020**, 369, 979.
- [28] A. VahidMohammadi, J. Rosen, Y. Gogotsi, *Science* **2021**, 372, eabf1581.
- [29] Y. Qin, T. Yu, S. Deng, X. Zhou, D. Lin, Q. Zhang, Z. Jin, D. Zhang, Y. He, H. Qiu, L. He, F. Kang, K. Li, T. Zhang, *Nat. Commun.* **2023**, 13, 3784.
- [30] X. Wang, D. Luo, J. Wang, Z. Sun, G. Cui, Y. Chen, T. Wang, L. Zheng, Y. Zhao, L. Shui, G. Zhou, K. Kempa, Y. Zhang, Z. Chen, *Angew. Chem., Int. Ed.* **2021**, 60, 2371.
- [31] F. Zuo, L. Wang, T. Wu, Z. Y. Zhang, D. Borchardt, P. Y. Feng, *J. Am. Chem. Soc.* **2010**, 132, 11856.
- [32] H. Niu, H. Zhou, H. Shao, H. Wang, X. Ding, R. Bai, T. Lin, *Nano Energy* **2021**, 90, 106618.
- [33] C. Mao, W. Zhu, Y. Xiang, Y. Zhu, J. Shen, X. Liu, S. Wu, K. M. C. Cheung, K. W. K. Yeung, *Adv. Sci.* **2021**, 8, 2002211.
- [34] K. Su, L. Tan, X. Liu, Z. Cui, Y. Zheng, B. Li, Y. Han, Z. Li, S. Zhu, Y. Liang, X. Feng, X. Wang, S. Wu, *ACS Nano* **2020**, 14, 2077.
- [35] J. Quan, F. Muttaqien, T. Kondo, T. Kozarashi, T. Mogi, T. Imabayashi, Y. Hamamoto, K. Inagaki, I. Hamada, Y. Morikawa, J. Nakamura, *Nat. Chem.* **2019**, 11, 722.
- [36] Y. Nosaka, A. Y. Nosaka, *Chem. Rev.* **2017**, 117, 11302.
- [37] J. S. Adams, A. Chemburkar, P. Priyadarshini, T. Ricciardulli, Y. B. Lu, V. Maliekkal, A. Sampath, S. Winikoff, A. M. Karim, M. Neurock, D. W. Flaherty, *Science* **2021**, 371, 626.
- [38] S. Yuan, J. Peng, B. Cai, Z. Huang, A. T. Garcia-Esparza, D. Sokaras, Y. Zhang, L. Giordano, K. Akkiraju, Y. G. Zhu, R. Hubner, X. Zou, Y. Roman-Leshkov, Y. Shao-Horn, *Nat. Mater.* **2022**, 21, 673.
- [39] R. Gao, J. Wang, Z.-F. Huang, R. Zhang, W. Wang, L. Pan, J. Zhang, W. Zhu, X. Zhang, C. Shi, J. Lim, J.-J. Zou, *Nat. Energy* **2021**, 6, 614.
- [40] S. Grimme, S. Ehrlich, L. Goerigk, *J. Comput. Chem.* **2011**, 32, 1456.
- [41] J. Zhou, B. Liao, B. Qiu, S. Huberman, K. Esfarjani, M. S. Dresselhaus, G. Chen, *Proc. Natl. Acad. Sci. U. S. A.* **2015**, 112, 14777.
- [42] L. Z. Su, D. Y. Wang, S. N. Wang, B. C. Qin, Y. P. Wang, Y. X. Qin, Y. Jin, C. Chang, L. D. Zhao, *Science* **2022**, 375, 1385.
- [43] C. Trilleaud, V. Gauttier, K. Biteau, I. Girault, L. Belarif, C. Mary, S. Pengam, G. Teppaz, V. Thepenier, R. Danger, G. Robert-Siegwald, M. Neel, S. Bruneau, A. Glemain, A. Neel, A. Poupon, J. F. Mosnier, G. Chene, M. Dubourdeau, G. Blanche, B. Vanhove, N. Poirier, *Sci. Adv.* **2021**, 7, eabd1453.
- [44] C. M. Hu, R. H. Fang, J. Copp, B. T. Luk, L. Zhang, *Nat. Nanotechnol.* **2013**, 8, 336.
- [45] J. Fu, Y. Li, Y. Zhang, Y. Liang, Y. Zheng, Z. Li, S. Zhu, C. Li, Z. Cui, S. Wu, *Adv. Mater.* **2021**, 33, 2102926.
- [46] Z. Wang, X. Gu, B. Li, J. Li, F. Wang, J. Sun, H. Zhang, K. Liu, W. Guo, *Adv. Mater.* **2022**, 34, 2204590.
- [47] J. S. del Río, O. Y. F. Henry, P. Jolly, D. E. Ingber, *Nat. Nanotechnol.* **2019**, 14, 1143.
- [48] Y. Y. Fu, J. Wang, B. H. Zhou, A. Pajulas, H. Y. Gao, B. Ramdas, B. Koh, B. J. Ulrich, S. S. Yang, R. Kapur, J. C. Renaud, S. Paczesny, Y. L. Liu, R. M. Tighe, P. Licon-Limon, R. A. Flavell, S. Takatsuka, D. Kitamura, R. S. Tepper, J. Sun, M. H. Kaplan, *Sci. Immunol.* **2022**, 7, eabi9768.
- [49] S. D. Mesquita, J. Herz, M. Wall, T. Dykstra, K. A. de Lima, G. T. Norris, N. Dabhi, T. Kennedy, W. Baker, J. Kipnis, *Sci. Adv.* **2021**, 7, eabe4601.
- [50] M. A. Fernandez-Yague, L. A. Hymel, C. E. Olingy, C. McClain, M. E. Ogle, J. R. Garcia, D. Minshew, S. Vyshnya, H. S. Lim, P. Qiu, A. J. Garcia, E. A. Botchwey, *Sci. Adv.* **2022**, 8, eabd8056.
- [51] D. A. C. Stapels, P. W. S. Hill, A. J. Westermann, R. A. Fisher, T. L. Thurston, A. E. Saliba, I. Blommestein, J. Vogel, S. Helaine, *Science* **2018**, 362, 1156.
- [52] S. A. Eming, T. A. Wynn, P. Martin, *Science* **2017**, 356, 1026.
- [53] E. A. Masters, B. F. Ricciardi, K. L. M. Bentley, T. F. Moriarty, E. M. Schwarz, G. Muthukrishnan, *Nat. Rev. Microbiol.* **2022**, 20, 385.
- [54] X. Pang, Q. Xiao, Y. Cheng, E. Ren, L. Lian, Y. Zhang, H. Gao, X. Wang, W. Leung, X. Chen, G. Liu, C. Xu, *ACS Nano* **2019**, 13, 2427.
- [55] J. Fu, T. Li, Y. Zhu, Y. Hao, *Adv. Funct. Mater.* **2019**, 29, 1906195.
- [56] Y. Dong, S. Dong, B. Liu, C. Yu, J. Liu, D. Yang, P. Yang, J. Lin, *Adv. Mater.* **2021**, 33, 2106838.
- [57] Y. Q. Qiao, X. M. Liu, B. Li, Y. Han, Y. F. Zheng, K. W. K. Yeung, C. Y. Li, Z. D. Cui, Y. Q. Liang, Z. Y. Li, S. L. Zhu, X. B. Wang, S. L. Wu, *Nat. Commun.* **2020**, 11, 4446.
- [58] O. Gordon, D. E. Lee, B. Liu, B. Langevin, A. A. Ordonez, D. A. Dikeman, B. Shafiq, J. M. Thompson, P. D. Sponseller, K. Flavahan, M. A. Lodge, S. P. Rowe, R. F. Dannals, C. A. Ruiz-Bedoya, T. D. Read, C. A. Peloquin, N. K. Archer, L. S. Miller, K. M. Davis, J. V. S. Gobburu, S. K. Jain, *Sci. Transl. Med.* **2021**, 13, eabl6851.
- [59] B. D. Gimza, J. E. Cassat, *Front. Immunol.* **2021**, 12, 638085.
- [60] T. Nakatsuji, H. I. Chiang, S. B. Jiang, H. Nagarajan, K. Zengler, R. L. Gallo, *Nat. Commun.* **2013**, 4, 1431.
- [61] M. Brummerstedt, M. Bangstrup, T. S. Barfod, *Spinal Cord Ser. Cases* **2018**, 4, 59.
- [62] Z. Wang, J. Li, J. Cho, A. B. Malik, *Nat. Nanotechnol.* **2014**, 9, 204.